FOI-R--1483--SE
Dcember 2004
ISSN 1650-1942
**Technical report**

# Sound absorption by viscoelastic coatings with periodically distributed cavities

Sven Ivansson

Systems Technology
SE-172 90 Stockholm

SWEDISH DEFENCE RESEARCH AGENCY

FOI-R—1483--SE

December 2004

ISSN 1650-1942

**Technical report**

# Sound absorption by viscoelastic coatings with periodically distributed cavities

Sven Ivansson

| Issuing organization | Report number, ISRN | Report type |
|---|---|---|
| FOI – Swedish Defence Research Agency | FOI-R—1483--SE | Technical report |
| | **Research area code** | |
| Systems Technology | 4. C4ISR | |
| SE-17290 Stockholm | **Month year** | **Project no.** |
| Sweden | December 2004 | E6058 |
| | **Sub area code** | |
| | 43 Underwater surveillance sensors | |
| | **Sub area code 2** | |

| Author/s (editor/s) | Project manager |
|---|---|
| Sven Ivansson | Henrik Claesson |
| | **Approved by** |
| | Monica Dahlén |
| | **Sponsoring agency** |
| | Swedish armed forces |
| | **Scientifically and technically responsible** |
| | Sven Ivansson |


**Report title**

Sound absorption by viscoelastic coatings with periodically distributed cavities


**Abstract (not more than 200 words)**

Thin rubber layers with spherical cavities can be used to redistribute normally incident sonar energy in the transverse direction, where it suffers loss by anelastic absorption. This is the basis for an old idea for anechoic submarine coatings. In this report, the mechanism for the anechoic effect is studied theoretically and numerically. Observing that the reflectivity is an analytic function of the shear wave velocity of the rubber material, winding-number methods are applied to prove the existence of, and also to design, coatings with vanishing reflectivity at isolated frequencies. The spatial distribution of the absorption losses is determined, with the major part suffered in the vicinity of the cavities for compressional spherically symmetric waves. The viscoelastic shear properties of the rubber matrix material are crucial for generating this loss. The requirements for anechoism are specified using plane-wave concepts from the invariant embedding technique. A classical monopole resonance for a spherical cavity in a solid is fundamental in order to fulfil these requirements. An energy relation is derived that relates the anelastic loss in the rubber layer to loss by scattering from a single cavity. A factor is isolated that quantifies the effects of multiple scattering, which are noticeable.



**Keywords**

Riccati method, multiple scattering, absorption cross-section

| Further bibliographic information | Language English |
|---|---|
| | |

| ISSN 1650-1942 | Pages p.30 |
|---|---|
| | Price acc. to pricelist |

| Utgivare | Rapportnummer, ISRN | Klassificering |
|---|---|---|
| Totalförsvarets Forskningsinstitut - FOI | FOI-R—1483--SE | Teknisk rapport |
| | **Forskningsområde** | |
| Systemteknik | 4. Spaning och ledning | |
| 172 90 Stockholm | **Månad, år** | **Projektnummer** |
| | December 2004 | E6058 |
| | **Delområde** | |
| | 43 Undervattenssensorer | |
| | **Delområde 2** | |

| Författare/redaktör | Projektledare |
|---|---|
| Sven Ivansson | Henrik Claesson |
| | **Godkänd av** |
| | Monica Dahlén |
| | **Uppdragsgivare/kundbeteckning** |
| | Försvarsmakten |
| | **Tekniskt och/eller vetenskapligt ansvarig** |
| | Sven Ivansson |


**Rapportens titel (i översättning)**

Absorption av ljud med R-beläggningar med periodiskt fördelade kaviteter


**Sammanfattning (högst 200 ord)**

Tunna gummiskikt med sfäriska kaviteter kan användas för att omfördela infallande ljudenergi till de laterala riktningarna där den kan absorberas av gummit. Detta är grunden för R-beläggningar av Alberich-typ för ubåtar. I denna rapport studeras funktionsmekanismen teoretiskt och numeriskt. Reflektionskoefficienten för normalt infallande planvågor kan ses som en analytisk funktion av gummits skjuvmodul. Argumentprincipen används för att påvisa existensen av R-beläggningar med reflektivitet noll vid isolerade frekvenser. Absorptionsförlusternas fördelning i gummit studeras, nästan all absorption äger rum nära kaviteterna för sfäriskt symmetriska kompressions-vågor. Gummits viskoelastiska skjuvegenskaper är viktiga för att generera dessa förluster. Kraven för reflexfrihet specificeras med användande av begrepp från Riccati-tekniken för vågutbredning i skiktade medier. En klassisk monopol-resonans för en sfärisk kavitet i en solid är viktig för att uppfylla dessa krav. En energirelation härleds för förlusterna i gummit i termer av förlusterna genom spridning från en enskild kavitet. Effekterna av multipelspridning är märkbara, och de isoleras till en modulerande faktor.



**Nyckelord**

Riccati's metod, multipelspridning, absorptionstvärsnitt

| Övriga bibliografiska uppgifter | Språk Engelska |
|---|---|
| | |

| ISSN 1650-1942 | Antal sidor: 30 s. |
|---|---|
| Distribution enligt missiv | Pris: Enligt prislista |

## EXPANDED ABSTRACT (in Swedish)

Arbetet med R-beläggning (R = reflektionsdämpande) för ubåtar har fortsatts under året. Föreliggande rapport har skrivits, en teoretisk studie rörande funktionsmekanismen för R-beläggningar av "Alberich" typ. Riccatimodellering används, innebärande en analys av reflektion och transmission av planvågor samt en hopkoppling med sfäriska vågor runt spridarna i gummiskiktet. För fullständighetens skull inkluderas de grundläggande begreppen från avsnitten 2.1-2 i förra årets rapport [0] även här.

Ett typfall studeras med sfäriska kaviteter med radie 3 mm i ett kvadratiskt gitter med sidan $d = 44$ mm i ett 10 mm tjockt gummiskikt, se figuren nedan. I jämförelse med förra årets rapport studeras lägre frekvenser, och vattnet under stålplattan har för enkelhets skull utelämnats. Teoretiskt visas att man med väl valda realistiska skjuvvågsparametrar för gummit kan få total reflexutsläckning vid frekvensen 9 kHz. Vid denna frekvens motsvarar gummits tjocklek endast 6 % av våglängden. Naturligtvis kan resultaten skalas om, så att reflexutsläckning vid t.ex. 4.5 kHz kan fås med en 20 mm tjock beläggning.

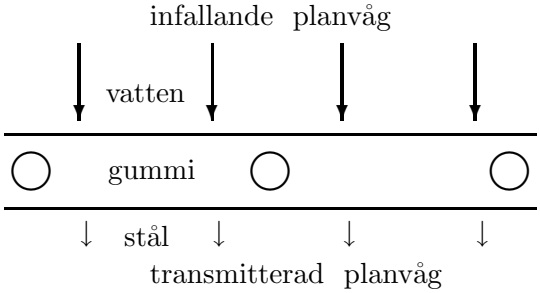


I rapporten tas detta exempel till utgångspunkt för en diskussion av mekanismen bakom reflexutsläckningen. Sett från den infallande planvågen upptar de sfäriska kaviteterna endast ung. 1.5 % av gummits tvärsnittsarea. Vidare är reflektionskoefficienten mot stålet ung. 0.94, och energiinnehållet i den till stålet transmitterade vågen blir mycket litet. Detta medför att varje kavitet måste bidra med ett mycket stort absorptionstvärsnitt, närmare 70 gånger den energi som infaller mot dess geometriska tvärsnittsarea måste absorberas. I rapporten illustreras hur denna absorption uppkommer genom ett energiflöde in mot kaviteterna. Ung. 71 % av förlusterna sker inom de 2.1 % av gummivolymen som ligger inom de 2 mm närmast sfärerna.

Det stora absorptionstvärsnitt som krävs uppkommer genom en välkänd resonans för spridning av radiellt symmetriska sfäriska kompressionsvågor (monopolspridning). Mot bakgrund av att endast skjuvvågsdämpning introducerats i gummimaterialet kunde man kanske ha väntat sig att en viktig komponent i förlustmekanismen skulle vara spridning i form av skjuvvågor, vilka sedan absorberas. Detta är alltså inte fallet. Att skjuvvågsdämpningen ändå kan orsaka kraftiga förluster för sfäriska kompressionsvågor nära spridaren förklaras av en av skjuvmodulen beroende spänning som verkar nära spridaren för att återställa de kraftiga laterala töjningar som där uppkommer. Denna återställande spänning saknas i en fluid.

Den använda beräkningsmetodiken medger en analys av inverkan av multipelspridning mellan kaviteterna. Speciellt härleds en energirelation där denna inverkan isoleras i en speciell faktor. Avståndet mellan kaviteterna är inte så stort relativt våglängden (ung. 27 %), och beräkningar utan hänsyn till multipelspridningen leder till att reflektionsminimum felaktigt förläggs till 7.7 i stället för 9 kHz.

Sammantaget resulterar monopolspridningen från gittrets kaviteter i planvågor uppåt och nedåt av lika amplitud. Reflexfrihet kräver då att den uppåtgående vågen och en från stålet reflekterad våg kan kancellera varann. Riccatitekniken används för att illustrera detta genom en expansion av reverberationsoperatorn. Alternativt skulle man kunna tänka sig en R-beläggning som byggde på att den infallande vågen kunde dämpas ut redan innan den nådde stålet.

Arbete med experimentell verifikation av de interferensfenomen som kan förväntas vid högre frekvenser, se avsnitt IV i rapporten, genomförs också under året. Vidare arbetar två examensarbetare med implementering

av moderna algoritmer för global optimering. Vår förhoppning är att få fram bättre verktyg för design av R-beläggningar än den tio år gamla genetiska algoritm som användes i förra årets rapport. Dessa aktiviteter är dock ännu ej avslutade, och de kommer att rapporteras på annat sätt. Studier av hårda spridare i gummiskiktet och spridare av mer allmän form samt bedömning av så kallade homogeniseringsansatser återstår att göra.

Till sist skall nämnas att arbetet med finita differenser för numerisk modellering av R-beläggningar har legat nere under året p.g.a. tjänstledighet (Lena Frenje-Lund).

**Referens**

[0] S. Ivansson och L. Frenje-Lund, "Modelling of echo reduction by Alberich anechoic coatings," FOI Rapport R–1039-SE (Stockholm, 2003).

# Sound absorption by viscoelastic coatings with periodically distributed cavities

Sven Ivansson

Division of Systems Technology
Swedish Defence Research Establishment
SE-172 90 Stockholm, Sweden

December 2004

**Abstract**

Thin rubber layers with spherical cavities can redistribute normally incident sonar energy in the transverse direction, where it suffers loss by anelastic absorption. This is the basis for an old idea for anechoic submarine coatings. Here, the anechoic effect is studied theoretically and numerically by adapting modern techniques for electron scattering and band gap computations for photonic and phononic crystals. Reflection and transmission matrices are computed recursively by invariant embedding, from basic such matrices for layers containing periodic arrays of cavities. Observing that the reflectivity is an analytic function of the shear wave velocity of the rubber material, winding-number methods are applied to prove the existence of, and to design, coatings with vanishing reflectivity at isolated frequencies. The spatial distribution of the absorption loss is determined, with the major part suffered in the vicinity of the cavities for compressional spherically symmetric waves. The viscoelastic shear properties of the rubber are crucial for generating this loss, although the generation of scattered shear waves turns out to be insignificant. The requirements for anechoism are specified using plane-wave concepts from the invariant embedding technique. A classical monopole resonance for a spherical cavity in a solid is fundamental in order to fulfil these requirements. An energy relation is derived that relates the anelastic loss in the rubber layer to loss by scattering from a single cavity. A factor is isolated that quantifies the effects of multiple scattering, which are noticeable.

## I. INTRODUCTION

Anechoic coatings for submarines, to avoid detection by an active sonar, have a long history and different types of coatings exist. Rubber coatings with air-filled cavities [1] were used already during the second world war. Such coatings are said to be of Alberich type, and an illustration is provided in Fig. 1. When sound from an active sonar enters the coating, part of it is scattered by the cavities. The scattered energy can subsequently be absorbed by the rubber material, and the amount of energy that is reflected back can be significantly reduced. Some ideas for the mechanisms of the echo reduction have been discussed by Gaunaurd *et al.* [2, 3, 4, 5] in connection with RST (resonance scattering theory). Scattering of compressional and shear waves by isolated spherical inclusions, including resonances, has also been treated by many other authors. [6, 7]

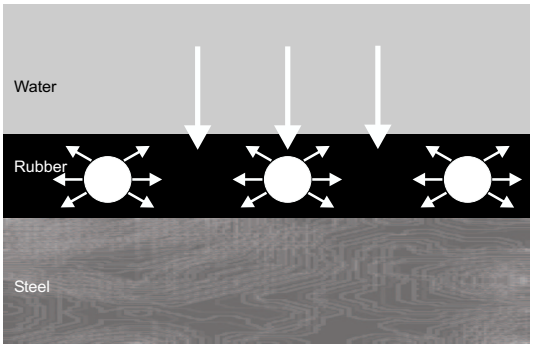


Figure 1: A steel plate is covered with an Alberich anechoic rubber coating. The arrows indicate incident sound from the water and some scattered waves.

A model for studying the performance of Alberich anechoic coatings was given by Oberst, [1] in terms of an equivalent electric circuit. Such circuits are common in noise technology. It is not apparent, however, how the mass, resistance and compliance parameters of such a model can be related to the sound velocities of the rubber material and the cavity radius, *etc.*

A theoretically more attractive approach is to apply wave propagation modeling, which is a well developed research area in underwater acoustics and seismology. [8, 9] At sufficiently low frequency, it may be possible to model the coating as a homogeneous viscoelastic layer, for which effective sound velocity and attenuation parameters may be determined. [10,11] Still, however, it is not apparent a priori how to relate the effective model parameters to the actual ones of the rubber material and the cavities.

The finite element method (FEM) has been used to incorporate details of the complicated sound scattering by the cavities. [12, 13, 14] An important advantage is the flexibility to model different types of Alberich coatings. Periodicity can be utilized to restrict the computer intensive FEM modeling to an individual unit cell.

The aim of the present paper is to study echo reduction by Alberich anechoic coatings with a faster semi-analytical method that has been borrowed from atomic physics and applied in recent years to studies of band gaps for photonic and phononic crystals. [15, 16] Indeed, sound scattering by the cavities within the rubber layer is formally related to electron scattering by atoms in a lattice. A computer implementation has been made, with an existing program for photonic crystals [17] (the electromagnetic case) as a very useful starting point, and the theory is briefly reviewed in Secs. II and III. Sound propagation through a sequence of layers, with or without cavities, may be handled recursively by a technique that is known in underwater acoustics and seismoacoustics as the invariant embedding or Riccati method. [8,18] It is for the treatment of the cavities that the techniques from atomic physics [19] become crucial, see Sec. III. The wave field scattered by each cavity is expanded in spherical wave functions, and an equation system is obtained for the coefficients. Convenient transformation formulas exist between spherical waves and plane waves, [20] which provides the coupling to the plane waves needed for the recursive invariant embedding treatment of multi-layered cases.

Basic examples of the effect of a periodic planar array of scatterers are given in Sec. IV. The energy of a normally incident plane wave is redistributed among plane waves in an infinite but discrete set of directions. At low frequency, all but the plane waves in the normal directions are evanescent. As the frequency is increased, more and more of these evanescent beams or plane waves become propagating.

A computational technique for coating design is presented in Sec. V. It is based on the observation that the reflection coefficient for specularly reflected waves into the water is analytic as a function of the shear modulus $\mu$ of the matrix material. Algorithms for finding zeroes of analytic functions can thus be applied to prove the existence of $(n.b.)$ and to design coatings with a reflectivity that vanishes exactly at a specified frequency. Absorption cross-sections and energy flux are computed and used to determine where the absorption loss is suffered.

Such a coating is subsequently analysed in detail in Sec. VI to provide an improved understanding of the mechanism for the Alberich anechoic effect. The shear properties of the rubber

material are not important for generating scattered shear waves, but for generating loss from scattered spherically symmetric compressional waves. This loss arises from a restoring stress close to the spherical cavities, that is absent in a fluid. An energy relation is derived, that identifies the absorption loss in the rubber layer with the loss induced by a single cavity, as modified by a multiplicative factor that includes effects of multiple scattering.

An attractive feature of the applied methodology is that the effects of multiple scattering can be assessed theoretically and quantified. The need for more research concerning multiple scattering corrections was in fact pointed out in a previous study. [21] Although not treated in the present paper, it would also be possible to assess the validity of homogenization or effective medium approaches. Some other ideas for future work and concluding remarks are provided in Sec. VII.

## II. THE INVARIANT EMBEDDING APPROACH

Consider a horizontal interface between two homogeneous solid or fluid half-spaces. A right-hand Cartesian $xyz$ coordinate system is assumed, with the $z$ axis pointing downwards and the $x$ axis pointing to the right. Waves with time dependence $\exp(-\mathrm{i}\omega t)$ are considered, where $\omega$ is the angular frequency.

In the solid case, a plane wave incident from above gives rise to three reflected and three transmitted waves,[9] since three different polarizations are possible (P, SV, SH). Since the incident plane wave may have three different polarizations as well, a 3×3 reflection-coefficient matrix $\mathcal{R}_B$ and a 3×3 transmission-coefficient matrix $\mathcal{T}_B$ may be formed, for complex displacement amplitudes. These matrices depend on the horizontal wavenumber, which is, however, constant among all seven waves according to Snell's law. For a plane wave incident from below, the matrices $\mathcal{R}_A$ and $\mathcal{T}_A$ are introduced analogously.

An "interface" at $z = 0$ is considered next, that does not represent a border between two different half-spaces but the plane of location for a two-dimensional periodic array of cavities or other scatterers, as illustrated in Fig. 2.

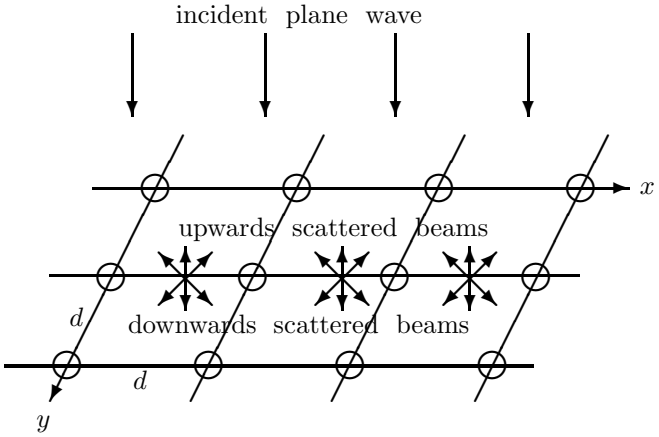


Figure 2: Scatterers in a lattice in the plane $z = 0$. The simple scatterer lattice redistributes some of the energy of the normally incident plane wave, in the positive $z$ direction, to non-normal directions.

The centers of the scatterers have $xy$ coordinates given by

$$\mathbf{R} = (x, y, 0) = m \cdot (d, 0, 0) + n \cdot (0, d, 0) \quad (1)$$

where $m$,$n$ are integers and $d$ is the period of the square scatterer lattice. It is convenient to introduce the reciprocal lattice in the wavenumber domain as well:

$$\mathbf{g} = (k_x, k_y, 0) = m \cdot (2\pi/d, 0, 0) + n \cdot (0, 2\pi/d, 0) \ . \quad (2)$$

Outside a layer containing the scatterers, plane-wave representations of the field are still valid. Hence, R/T (reflection/transmission) matrices $\mathcal{R}_B$,$\mathcal{T}_B$ and $\mathcal{R}_A$,$\mathcal{T}_A$ can still be introduced. However, reflected and transmitted waves with different horizontal wavenumbers than that of the incident wave, which is written as the vector $\mathbf{k}_{||}$, may now appear. For each field variable $\varphi(x, y, z)$, $\exp(-\mathrm{i} \cdot \mathbf{k}_{||} \cdot (x, y, 0)) \cdot \varphi(x, y, z)$ may for each fixed $z$ be expanded in a Fourier series

in $x$ and $y$. Hence, it is the discrete set of horizontal wavenumbers $\mathbf{k}_{||}+\mathbf{g}$, where $\mathbf{g}$ belongs to the reciprocal lattice of Eq. (2), that may now appear. Illustrations are attempted in Figs. 2 and 3.

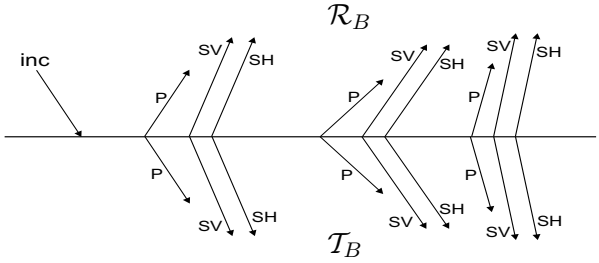


Figure 3: A plane wave incident on periodically distributed scatterers in the plane $z = 0$ gives rise to reflected and transmitted P,SV,SH waves of different horizontal wavenumbers. Different $y$ components appear as well, although this is not clearly illustrated in this $xz$ diagram.

Specifically, with the time dependence $\exp(-\mathrm{i}\omega t)$ suppressed as usual, the displacement vector for each incident, reflected or transmitted plane wave is a multiple, given by the complex displacement amplitude, of

$$\mathbf{u}(\mathbf{r}) = \exp(\mathrm{i}\,\mathbf{K}^s_{\mathbf{g}j}\cdot\mathbf{r})\cdot\mathbf{e}_j\ . \tag{3}$$

Here, $\mathbf{r} = (x, y, z)$, $s = +(-)$ for a wave incident from above (below), while $j$ = 1,2,3 for a wave of type P,SV,SH, respectively. Furthermore,

$$\begin{aligned}\mathbf{K}^{\pm}_{\mathbf{g}j} &= \mathbf{k}_{||}+\mathbf{g}\ \pm \\ &\quad [\omega^2/c_j^2 - |\mathbf{k}_{||}+\mathbf{g}|^2]^{1/2}\cdot(0,0,1) \quad (4)\\ &= \frac{\omega}{c_j}\,(\sin\theta\cos\phi, \sin\theta\sin\phi, \cos\theta) \quad (5)\end{aligned}$$

where $c_j$ is the compressional-wave velocity $\alpha$ when $j = 1$ and the shear-wave velocity $\beta$ when $j = 2, 3$, while the angular variables $\theta$, $\phi$ of $\mathbf{K}^{\pm}_{\mathbf{g}j}$ are defined by Eq. (5), with a possibly complex $\cos\theta$. In the viscoelastic case, with a complex $c_j$, $\sin\theta$ is complex as well but the quotient $\sin\theta/c_j$ remains real. The polar vectors $\mathbf{e}_j = \mathbf{e}_j(\mathbf{K}^{\pm}_{\mathbf{g}j})$, finally, are defined as usual by $\mathbf{e}_1 = (\sin\theta\cos\phi, \sin\theta\sin\phi, \cos\theta)$, $\mathbf{e}_2 = (\cos\theta\cos\phi, \cos\theta\sin\phi, -\sin\theta)$, $\mathbf{e}_3 = (-\sin\phi, \cos\phi, 0)$.

Several interfaces are involved in Fig. 1, with as well as without scatterers, and R/T matrices for different interfaces have to be combined. This combination can be performed recursively. It is sufficient to consider the case with two interfaces as shown in Fig. 4. Incorporating layer thicknesses by appropriate

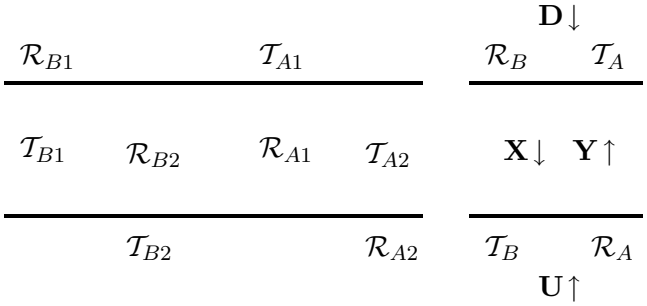


Figure 4: R/T matrices $\mathcal{R}_{B1}$,$\mathcal{T}_{B1}$, $\mathcal{R}_{A1}$,$\mathcal{T}_{A1}$ and $\mathcal{R}_{B2}$,$\mathcal{T}_{B2}$, $\mathcal{R}_{A2}$,$\mathcal{T}_{A2}$ for an upper and a lower interface, respectively, may be combined to form the total R/T matrices $\mathcal{R}_B$,$\mathcal{T}_B$, $\mathcal{R}_A$,$\mathcal{T}_A$. The complex displacement amplitude vectors $\mathbf{D}$, $\mathbf{U}$, $\mathbf{X}$, and $\mathbf{Y}$ for Eqs. (9)-(12) are also included.

phase shifts, which is easily done for plane waves as in Eq. (3), the following formulas are easily established: [19, 18]

$$\begin{aligned}\mathcal{R}_B &= \mathcal{R}_{B1} + \mathcal{T}_{A1}\cdot \\ &\qquad [\mathbf{I} - \mathcal{R}_{B2}\cdot\mathcal{R}_{A1}]^{-1}\cdot\mathcal{R}_{B2}\cdot\mathcal{T}_{B1} \quad (6)\\ &= \mathcal{R}_{B1} + \mathcal{T}_{A1}\cdot\mathcal{R}_{B2}\cdot \\ &\qquad [\mathbf{I} - \mathcal{R}_{A1}\cdot\mathcal{R}_{B2}]^{-1}\cdot\mathcal{T}_{B1} \quad (7)\\ \mathcal{T}_B &= \mathcal{T}_{B2}\cdot[\mathbf{I} - \mathcal{R}_{A1}\cdot\mathcal{R}_{B2}]^{-1}\cdot\mathcal{T}_{B1}\ , \quad (8)\end{aligned}$$

where each $\mathbf{I}$ denotes the appropriate identity matrix. Formulas for $\mathcal{R}_A$,$\mathcal{T}_A$ are analogous. Numerical stability is achieved, since increasing exponentials are absent. Similar formulas apply in the context of an invariant embedding or Riccati method for solving general boundary-value problems for systems of ordinary differential equations. [22]

For the situation in Fig. 4, there is a simple method to determine the solution at the inter-

mediate level when the wave field at the upper and lower levels has been computed. Complex displacement amplitudes are denoted by **D** (downgoing at the upper level), **U** (upgoing at the lower level), **X** (downgoing at the intermediate level), and **Y** (upgoing at the intermediate level), as illustrated in the figure. The following relations are readily established:

$$\mathbf{Y} = \mathcal{R}_{B2}\cdot\mathbf{X} + \mathcal{T}_{A2}\cdot\mathbf{U} \quad (9)$$

$$\mathbf{X} = \mathcal{R}_{A1}\cdot\mathbf{Y} + \mathcal{T}_{B1}\cdot\mathbf{D}\ . \quad (10)$$

The linear equation systems for determination of **X** and **Y** become

$$(\mathbf{I} - \mathcal{R}_{A1}\cdot\mathcal{R}_{B2})\cdot\mathbf{X} = \mathcal{T}_{B1}\cdot\mathbf{D} + \mathcal{R}_{A1}\cdot\mathcal{T}_{A2}\cdot\mathbf{U} \quad (11)$$

$$(\mathbf{I} - \mathcal{R}_{B2}\cdot\mathcal{R}_{A1})\cdot\mathbf{Y} = \mathcal{T}_{A2}\cdot\mathbf{U} + \mathcal{R}_{B2}\cdot\mathcal{T}_{B1}\cdot\mathbf{D}\ . \quad (12)$$

## III. R/T MATRICES FOR AN INTERFACE WITH PERIODICALLY DISTRIBUTED SCATTERERS

Explicit expressions for the R/T matrices introduced in Sec. II are well known for an interface between two homogeneous half-spaces. [9] Only plane-wave field representations are needed, since the wave equations are separable in Cartesian coordinates. A two-dimensional spatial Fourier transform is appropriate, from $xy$ to $k_x k_y$. The vertical wavenumbers $k_z$, *cf.* Eq. (4), are determined to achieve fulfilment of the wave equations.

The wave equations are separable in spherical coordinates as well, which is useful for handling an interface with periodically distributed scatterers. Angular dependence is expressed in terms of vector spherical harmonics that are orthonormal on the unit sphere. [9] As in Ref. [16], for example, the following basic spherical vector solutions to the wave equations for the displacement vector **u** are used:

$$\mathbf{u}^L_{lm}(\mathbf{r}) = \frac{\alpha}{\omega}\cdot\nabla\left(f_l(\omega r/\alpha)Y_l^m(\theta,\phi)\right) \quad (13)$$

$$\mathbf{u}^M_{lm}(\mathbf{r}) = \mathrm{i}f_l(\omega r/\beta)\cdot\frac{1}{\sqrt{l(l+1)}}\cdot \left(\frac{1}{\sin\theta}\frac{\partial Y_l^m(\theta,\phi)}{\partial\phi}\cdot\mathbf{e}_2(\mathbf{r}) - \frac{\partial Y_l^m(\theta,\phi)}{\partial\theta}\cdot\mathbf{e}_3(\mathbf{r})\right) \quad (14)$$

$$\mathbf{u}^N_{lm}(\mathbf{r}) = \frac{\mathrm{i}\beta}{\omega}\cdot\nabla\times\mathbf{u}^M_{lm}(\mathbf{r}) \quad (15)$$

where $\theta$,$\phi$ are the angular variables of $\mathbf{r}$ and $r = |\mathbf{r}|$. $Y_l^m = Y_l^m(\theta,\phi)$ are the surface spherical harmonics. The index $l$=0,1,2,.. with $m$=-$l$,..,$l$, but it is understood that $\mathbf{u}^M_{00} \equiv \mathbf{u}^N_{00} \equiv \mathbf{0}$. In order to fulfil the wave equations, there are two basic options: the function $f_l$ is either taken as the spherical Bessel function $\mathrm{j}_l$ or as the spherical Hankel function $\mathrm{h}_l^+$. The notation $\mathbf{u}^{0L}_{lm}$,$\mathbf{u}^{0M}_{lm}$,$\mathbf{u}^{0N}_{lm}$ and $\mathbf{u}^{+L}_{lm}$,$\mathbf{u}^{+M}_{lm}$,$\mathbf{u}^{+N}_{lm}$ is used for the two cases, respectively. Dimensions appear in expansion coefficients, and these vectors are actually dimensionless.

The outgoing field from each individual scatterer can be expanded in terms of $\mathbf{u}^{+P}_{lm}$, where $P = L, M, N$. For the scatterer centered at the origin, the scattered field is thus written

$$\mathbf{u}_{sc,\mathbf{0}}(\mathbf{r}) = \sum_{Plm} b^{+P}_{lm}\ \cdot\ \mathbf{u}^{+P}_{lm}(\mathbf{r})\ . \quad (16)$$

For a linear combination of plane waves, Eq. (3), incident on the scatterer lattice, the expansion coefficients for different scatterers are related by simple phase factors because of periodicity. Thus, the total scattered field $\mathbf{u}_{sc}$ is written [16]

$$\mathbf{u}_{sc}(\mathbf{r}) = \sum_{Plm}\left(b^{+P}_{lm}\sum_{\mathbf{R}}\mathrm{e}^{\mathrm{i}\cdot\mathbf{k}_{||}\cdot\mathbf{R}}\cdot\mathbf{u}^{+P}_{lm}(\mathbf{r}-\mathbf{R})\right), \quad (17)$$

where the sum on **R** is taken over lattice vectors **R** according to Eq. (1).

In order to obtain the R/T matrices, the expansion of Eq. (17) must be transformed to plane waves as written in Eq. (3). The following relation is crucial for this purpose: [16]

$$\sum_{\mathbf{R}}\mathrm{e}^{\mathrm{i}\cdot\mathbf{k}_{||}\cdot\mathbf{R}}\cdot\mathrm{h}_l^+(\omega|\mathbf{r}-\mathbf{R}|/c_j)\cdot Y_l^m(\hat{\mathbf{r}-\mathbf{R}}) = \sum_{\mathbf{g}}\frac{2\pi(-\mathrm{i})^l c_j}{\omega d^2 K^+_{\mathbf{g}jz}}\cdot Y_l^m(\hat{\mathbf{K}^{\pm}_{\mathbf{g}j}})\cdot\mathrm{e}^{\mathrm{i}\mathbf{K}^{\pm}_{\mathbf{g}j}\cdot\mathbf{r}}\ . \quad (18)$$

Here, $\mathbf{K}^+_{\mathbf{g}j}$ should be used for $z > 0$ while $\mathbf{K}^-_{\mathbf{g}j}$ is needed for $z < 0$. A caret indicates the angular

variables of the indicated quantity, and $K^+_{\mathbf{g}jz}$ denotes the $z$ component of $\mathbf{K}^+_{\mathbf{g}j}$. A proof can be found on p. 75-80 of Ref. [19]. For $l = m = 0$, Eq. (18) is readily derived from the Weyl integral[9] with the aid of the Poisson sum formula in two dimensions.

With the aid of Eq. (18), a plane-wave representation of Eq. (17) is easily obtained [15] by expressing derivatives of $Y_l^m$ in terms of itself and $Y_l^{m\pm1}$. As anticipated from Sec. II, it is the reciprocal lattice of Eq. (2) that provides the changes of the horizontal wavenumbers.

The only remaining task is to compute the expansion coefficients $b^{+P}_{lm}$ appearing in Eq. (17). These coefficients represent the outgoing (scattered) field from the scatterer centered at the origin. The main steps are now indicated, as given in more detail in Ref. [16], for an approch that takes multiple scattering into account in a self-consistent way. Multiple scattering can be important, since scattering may be favored at certain frequencies by lattice resonances [23] in addition to the single-scattering resonances. [5]

The incoming field on the scatterer centered at the origin, for example, has two parts: the incoming plane waves from adjacent layers written as a linear combination of basic plane waves according to Eq. (3), and the outgoing (scattered) field from all the other scatterers. Both these fields can be expanded in terms of $\mathbf{u}^{0P}_{lm}$. The expansion coefficients for the former are here denoted $a^{0P}_{lm}$, explicit expressions are derived in Liu *et al.*, [15] for example, while those for the latter are here denoted $b'^{P}_{lm}$. Hence, this incoming field is

$$\mathbf{u}_{inc,\mathbf{0}}(\mathbf{r}) \;=\; \sum_{Plm} (a^{0P}_{lm} + b'^{P}_{lm}) \cdot \mathbf{u}^{0P}_{lm}(\mathbf{r}) \;. \quad (19)$$

A T-matrix (transition matrix) argument immediately provides the equation system

$$b^{+P}_{lm} = \sum_{P'l'm'} T^{PP'}_{lm;l'm'} \cdot (a^{0P'}_{l'm'} + b'^{P'}_{l'm'}) \;, \quad (20)$$

where explicit expressions exist for the T-matrix $T^{PP'}_{lm;l'm'}$ for a spherical scatterer. [2, 5, 16] A second equation system can be derived by translating each wave $b^{+P}_{lm} \cdot \mathbf{u}^{+P}_{lm}(\mathbf{r} - \mathbf{R})$ to the origin: [16]

$$b'^{P}_{lm} = \sum_{P'l'm'} \Omega^{PP'}_{lm;l'm'} \cdot b^{+P'}_{l'm'} \;, \quad (21)$$

where the matrix $\Omega^{PP'}_{lm;l'm'}$ depends on $d \cdot \mathbf{k}_{||}$ and $\omega d/\alpha$, $\omega d/\beta$.

Elimination of $b'^{P}_{lm}$ between Eqs. (20) and (21) provides the desired equation system for $b^{+P}_{lm}$. For spherical scatterers, a useful feature is that the equation system splits in two subsystems. [19] It follows that Eq. (17) is valid outside the spherical scatterers, since all boundary conditions, radiation conditions and wave equations are fulfilled. Being based on Eq. (17) together with Eq. (18), the plane-wave representation is valid outside the spherical scatterers for nonzero $z$.

A single-scattering approximation is implemented by ignoring the $b'^{P'}_{l'm'}$ contribution in Eq. (20). In this case, the expansion coefficients $b^{+P}_{lm}$ are readily obtained from the T-matrix without any need to solve an equation system.

The time-averaged acoustic power that is reflected back into the water can be computed from the overall reflection matrix $\mathcal{R}_B$ for the complete fluid-solid structure, *cf.* Fig. 1. This computation involves intensity or energy flux integration over lateral position. Such integration or averaging implies under fairly general conditions that cross-terms, which appear when the quadratic energy flux expression is formed, can be ignored. This is discussed in detail in Appendix A. For the examples in Secs. V and VI, however, there is in general only one propagating reflected wave in the water.

## IV. REDISTRIBUTION OF ENERGY TO NONSPECULAR DIRECTIONS

The fundamental property of scatterers in a periodic planar lattice, to redistribute incoming plane-wave energy in an infinite but discrete set of directions, has been illustrated in Figs. 2 and 3. The phenomenon is related to the Fraunhofer diffraction patterns for a multiple-

slit aperture in optics. [24]

An example of the type shown in Fig. 1 is considered, with a 10 mm thick rubber coating. The water sound velocity and density are 1480 m/s and 1.0 kg/dm$^3$, respectively, as are the corresponding rubber material parameters. Direct reflections at the water/rubber interface are thus avoided at normal incidence. Below the coating, there is a steel half-space with density 7.7 kg/dm$^3$, compressional-wave velocity 5850 m/s, and shear-wave velocity 3230 m/s. Only the rubber is anelastic. It is modeled as a viscoelastic solid with shear-wave velocity and absorption given by 100 m/s and 17.5 dB/wavelength, respectively. For simplicity of forthcoming analysis in Sec. VI, vanishing rubber compressional-wave absorption is assumed. The cavities are spherical with a radius of 3 mm and evacuated (air filling would produce almost identical results). They are distributed in the middle of the coating in a square lattice with period $d = 44$ mm.

A plane-wave pulse is normally incident on the scatterer plane, chosen as $z = 0$. By Fourier synthesis, the backscattered pressure field is computed as nine time traces. These nine traces correspond to receivers in the water at a distance of 1 m from the water/rubber interface, uniformly spaced from $(x, y) = (-d/2, 0)$ to $(x, y) = (+d/2, 0)$ along a horizontal period $d$ with the central receiver directly above a spherical scatterer at $(x, y) = (0, 0)$.

At first, the case is considered when the spectrum of the incident plane-wave pulse is in the band 20-30 kHz. As verified from Eqs. (2)-(4), only the specularly reflected beam in the water is propagating in this case. At the distance considered, all evanescent waves have died out. As seen in the upper panel of Fig. 5, the backscattered pressure field has a very simple appearance without variation in the horizontal direction. The shapes of the reflected and incident pressure pulses are identical.

By increasing the pulse frequencies to get a spectrum essentially in the band 35-45 kHz, five beams become propagating. These are the beams with ($m$,$n$) = (0,0), (1,0), (-1,0), (0,1), and (0,-1) according to Eq. (2). The four non-

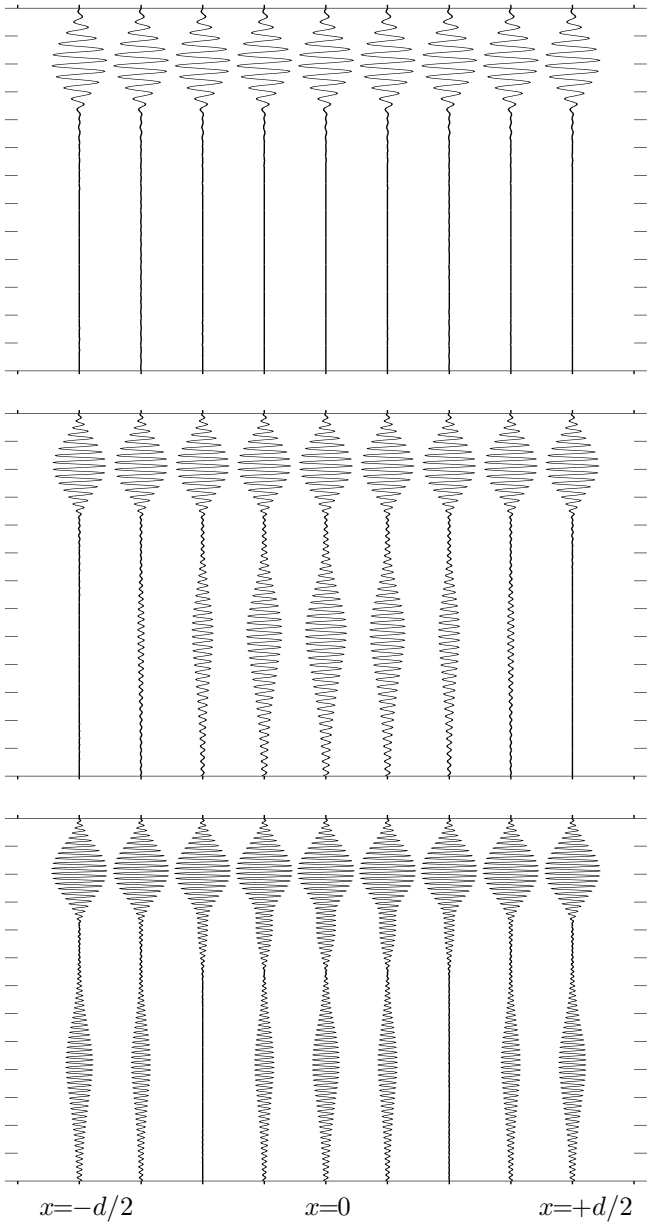


Figure 5: Time traces for the backscattered pressure field 1 m into the water for a coating of the type shown in Fig. 1, as described in the text. The normally incident plane-wave pulse has its spectrum in the band 20-30 kHz (upper panel), 35-45 kHz (middle panel), and 50-60 kHz (lower panel). Time increases downwards in each panel, starting 0.5 ms after the arrival of the center of the incident pulse at the water/rubber interface, and there is 0.1 ms between tick marks.

specularly reflected beams interact to create a pattern of constructive and destructive interference along the horizontal direction, middle panel of Fig. 5. Recalling that the pressure $p$ in a fluid with density $\rho$ and sound velocity $c$ equals $-\rho c^2 (\nabla \cdot \mathbf{u})$, it follows from Eqs. (2)-(4) that the $xy$ dependence of the pressure contribution by the beam quartet is given by

$$\exp(\mathrm{i}\tfrac{2\pi x}{d}) + \exp(-\mathrm{i}\tfrac{2\pi x}{d}) + \exp(\mathrm{i}\tfrac{2\pi y}{d}) + \exp(-\mathrm{i}\tfrac{2\pi y}{d}) \;=\; 2\left(\cos\tfrac{2\pi x}{d} + \cos\tfrac{2\pi y}{d}\right) . \quad (22)$$

A vanishing contribution appears at $(x, y) = (\pm d/2, 0)$ while maxima appear at $(x, y) = (0, 0)$, for example, which is precisely what can be observed in the middle panel of Fig. 5. The vertical wavenumber $k_z$ of the beam quartet is

$$k_z = \sqrt{\omega^2/c^2 - (2\pi/d)^2} \; , \quad (23)$$

as obtained from Eqs. (2)-(4), corresponding to a late slanting arrival with vertical group velocity

$$\frac{d\omega}{dk_z} \;=\; c\sqrt{1 - \left(\frac{2\pi}{d}\,\frac{c}{\omega}\right)^2} \; . \quad (24)$$

Finally, the frequency band 50-60 kHz is considered for the pulse spectrum. Another beam quartet becomes propagating, the one with $(m,n) = (1,1)$, $(-1,1)$, $(1,-1)$, and $(-1,-1)$ according to Eq. (2). In the lower panel of Fig. 5, arrivals can be identified that correspond to the specular beam and this new beam quartet. The previous beam quartet can be seen as well, although it interferes with the specular beam because of a small time separation at the distance 1 m. Again, the beams within a quartet interact to create a pattern of constructive and destructive interference along the horizontal direction. The $xy$ dependence of the pressure contribution by the new beam quartet becomes

$$\exp(\mathrm{i}\tfrac{2\pi(x+y)}{d}) + \exp(-\mathrm{i}\tfrac{2\pi(x-y)}{d}) + \exp(\mathrm{i}\tfrac{2\pi(-x-y)}{d}) + \exp(-\mathrm{i}\tfrac{2\pi(-x+y)}{d}) \;=\; 4\cos\tfrac{2\pi x}{d}\cos\tfrac{2\pi y}{d} \; . \quad (25)$$

Vanishing contributions appear at $(x, y) = (\pm d/4, 0)$, while maximal amplitudes appear at $(x, y) = (0, 0)$ and $(x, y) = (\pm d/2, 0)$, for example, which is precisely what can be observed in the lower panel of Fig. 5. The vertical wavenumber $k_z$ of the new beam quartet is

$$k_z = \sqrt{\omega^2/c^2 - 2(2\pi/d)^2} \quad (26)$$

with a corresponding vertical group velocity given by

$$\frac{d\omega}{dk_z} \;=\; c\sqrt{1 - 2\left(\frac{2\pi}{d}\,\frac{c}{\omega}\right)^2} \; . \quad (27)$$

Inserting $c = 1480$ m/s (the compressional-wave velocity of the water) and $d = 44$ mm (the lattice period), the late arrivals in the lower panel of Fig. 5 are predicted well.

In these examples, energy is sucked out of the specularly reflected beam and redistributed to other directions when propagating beams in nonspecular directions begin to exist in the water, as determined by the lattice. The effect is further illustrated in Fig. 6, which shows reflected power as a function of frequency. The most conspicuous feature for the total reflected power in curve (a) is the clear anechoic effect in an interval around 10 kHz. According to Eqs. (2)-(4), the beam quartets considered are introduced at $c/d = 33.6$ kHz, as shown by curve (c), and $c\sqrt{2}/d = 47.6$ kHz, as shown by curve (d).

Rather than obtaining anechoism by absorption of incident energy, it could be of interest to link the energy off in harmless nonspecular directions. Indeed, some further reductions in reflected power can be observed within the frequency intervals 34-47 kHz and 48-67 kHz for curve (b) of Fig. 6, where the energy in the nonspecular directions is ignored. The effect is small, however, and the corresponding specular reflections in Fig. 5 are only slightly reduced in amplitude in relation to the incident waves.

In all examples, *cf.* Fig. 1, the incident and reflected waves are studied in a fluid (water). For a solid, particularly one with a low shear velocity, propagating shear waves in nonspecular directions could appear at much lower frequencies. Still, however, it appears that the main

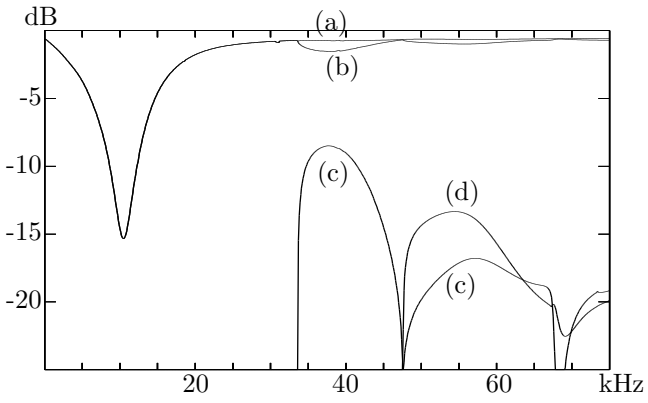


Figure 6: Reflected power as a function of frequency, in dB relative to the power of the normally incident plane wave. The coating is of the type shown in Fig. 1 with parameter values given in the text. The total reflected power is shown by curve (a). Curve (b), which coincides with curve (a) below 33 kHz, concerns the part in the specular beam. The contributions from the two beam quartets discussed in the text are shown by curves (c) and (d), respectively.

part of the reflected energy typically appears in the specular compressional-wave beam.

## V. COATING DESIGN USING ANALYTICITY OF THE REFLECTION COEFFICIENT

For a constant rubber density $\rho$, the specular plane-wave reflection coefficient for waves from the water, now denoted $\mathcal{R}$, is an analytic function of the shear modulus $\mu = \rho\beta^2$ of the rubber material. It is the complex shear velocity $\beta$ that is varied. The analyticity allows zeroes of $\mathcal{R}(\mu)$ to be identified by numerical winding-integral techniques,[25] whereby the argument variation of $\mathcal{R}$ is determined around search rectangles in the $\mu$ plane. Adaptive splitting of these search rectangles is applied, as illustrated in Fig. 7, until exactly one zero is enclosed. The secant method is finally used to refine the estimate of an isolated zero. During this process, the numerical evaluation of $\mathcal{R}$ at each $\mu$ is performed by the approach described in Secs. II and III.

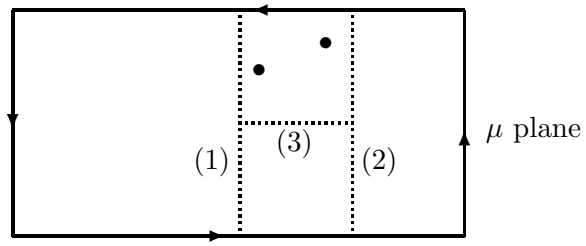


Figure 7: Adaptive splitting of search rectangles in the complex $\mu$ plane to locate zeroes of an analytic function by argument variation computations.

With carefully implemented error control, the existence of zeroes can actually be proved. The argument variation of $\mathcal{R}(\mu)$ around a closed path in the $\mu$ plane is an integral multiple of $2\pi$. The exact value is of course not obtained numerically, but a value close to $2\pi$, for example, implies that one zero is enclosed.

An example is now considered, of the type shown in Fig. 1. All parameters are kept at their values from the example in Sec. IV, except the rubber shear-wave velocity and absorption, which are varied to form a variable shear modulus $\mu$. The described technique was used to determine a $\mu$ value providing zero reflectivity for normally incident plane waves at 9 kHz. The computed $\mu$ corresponds to a rubber shear velocity and shear absorption of 83.6 m/s and 14.3 dB/wavelength, respectively. Fig. 8 shows the resulting curve for reflected power versus frequency.

The anechoic effect in Fig. 8 is due to the spherical inclusions and the shear wave absorption in the rubber. Without the cavities, $\mathcal{R}$ would be about 0.94, implying a reflection loss of about 0.6 dB (indicated in Fig. 8). Without the absorption, virtually all incident energy would of course be reflected back into the water by the rubber/steel interface, whether or not any cavities were present.

Comparison with the curve marked *s*, computed as indicated at the end of Sec. III, provides an assessment of the effect of multiple scattering among the cavities. A qualitatively similar result is obtained, but with the 9 kHz dip moved to 7.7 kHz. Although the lattice pe-

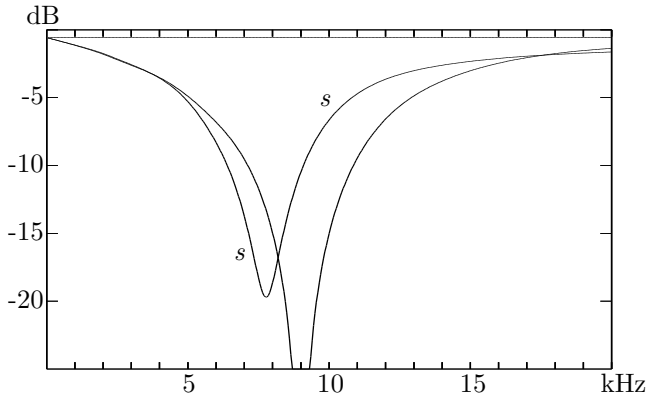


Figure 8: Reflected power as a function of frequency, in dB relative to the power of the normally incident plane wave. The 10 mm coating is of the type shown in Fig. 1, with cavity radius $a = 3$ mm and period $d = 44$ mm. The small (0.6 dB) reflection loss for a coating without cavities is indicated (the line at the top), and the curve marked $s$ concerns the single-scattering approximation result. The rubber $\mu$ was determined to achieve zero reflectivity at 9 kHz.

riod $d = 44$ mm is large in comparison to the cavity radius $a = 3$ mm, it is only about 27 % of the wavelength, and the single-scattering approximation leads to clearly noticeable errors.

Fig. 9 shows time domain results obtained by Fourier synthesis. A pulse with spectrum in the band 7-11 kHz was chosen (upper panel), for which significant echo reduction is anticipated according to Fig. 8. The reflected pulse as viewed at the water/rubber interface (middle panel) is weak except directly above a spherical scatterer at $(x, y) = (0, 0)$ (the central trace). The corresponding energy is built up by evanescent waves, however. It has disappeared already at a distance of 1 cm into the water, but the lower panel shows the results further away at a distance of 1 m. The horizontal line in each panel indicates the time at which the center of the symmetrical incident pulse has reached the water/rubber interface. The reflected pulse has been changed dramatically by this wave-theoretic notch filter, as seen in the lower panel. In the vicinity of 9 kHz, it appears that the pertinent transfer function is well approximated by a multiple of $(1-1.6\,\mathrm{i})\,(\omega-\omega_0)$, where $\omega_0 = 2\pi \cdot 9000$ Hz. Such a transfer function causes an apparent splitting of a pulse with symmetrical spectrum around 9 kHz, and this is precisely what can be observed in the lower panel of Fig. 9. A further discussion of this phenomenon is provided in Appendix B.

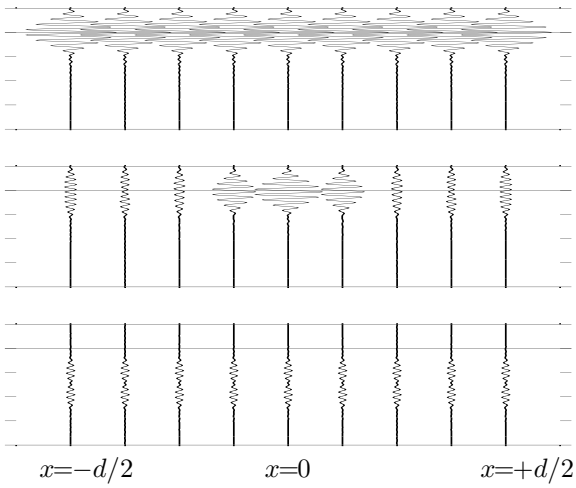


Figure 9: Results of pulse computations by frequency synthesis, corresponding to Fig. 8. The incident pulse is shown (upper panel) along with the reflected pulse as seen at the water/rubber interface (middle panel) and 1 m into the water (lower panel). Time increases downwards with 0.5 ms between tick marks and there is a horizontal line for a common reference time. Nine traces are drawn in each case, covering the overall period $d$=44 mm along the $x$ axis.

### A. Absorption loss

The loss by anelastic absorption is quantified in Fig. 10. It is readily determined by relating the intensities of the reflected (back into the water) and transmitted (into the steel) beams to the intensity of the incident beam. An effective normalized absorption cross-section per cavity, in the present context, appears by multiplying the intensity loss fraction by the geometrical cross-section ratio $d^2/\pi a^2 = 68.5$. As expected, *cf.* Fig. 8, a very large absorption cross-section appears around 9 kHz.

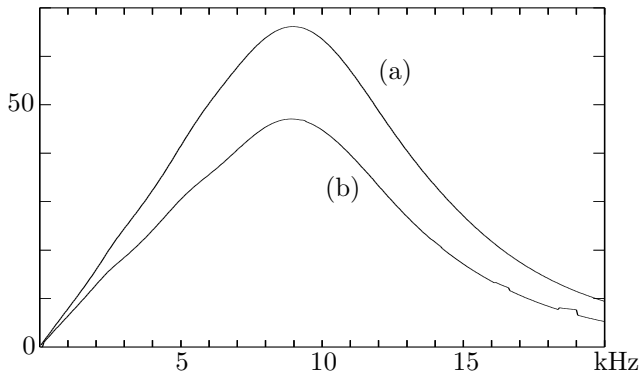


Figure 10: The upper curve (a) shows effective normalized absorption cross-section per cavity, corresponding to Fig. 8. The contribution to this cross-section from anelastic absorption within 2 mm of the spherical cavity is indicated by the lower curve (b).

Moreover, the computational techniques described in Secs. II and III allow a determination of the lossy parts of the rubber layer. The complex amplitudes of the plane waves that approach the cavities from above and below can be computed using Eqs. (9)-(12). These plane waves can subsequently be expanded in spherical waves, and equations for computing the anelastic loss within a specified volume are contained in Appendix C. The simplest case is a spherical region enclosing a cavity. A maximal radius of 5 mm is allowed in order not to touch the layer boundaries. The lower curve in Fig. 10 shows the contribution to the effective normalized absorption cross-section from the part of the rubber layer within 2 mm of a particular cavity. Indeed, the absorption loss is significant close to the cavities. In the present case, with $a = 3$ mm, $d = 44$ mm, and a rubber layer thickness of 10 mm, the specified cavity surroundings occupy only about 2.1 % of the rubber volume. It is remarkable that as much as about 71 % of the loss is suffered in such a small fraction of the volume, which is the case at 9 kHz, for example, according to Fig. 10.

### B. Energy flux

The results of Figs. 8 and 10 are now complemented by a study of the spatial distribution of the energy flux at 9 kHz. Fig. 11 shows the vertical component $\mathcal{F}_z(\mathbf{r})$ of the time-averaged energy flux vector $\mathcal{F}(\mathbf{r})$, see Eq. (61) of Appendix A. The horizontal axis indicates the horizontal distance from the scatterer at the origin, *cf.* Fig. 2. Results are given along two horizontal directions: the positive $x$ axis up to its point of symmetry at $x = d/2 = 22$ mm (right part), and the diagonal direction with $x = y$ up to its point of symmetry at $x = y = d/\sqrt{2} = 31.1$ mm (left part). Five curves are shown, corresponding to five different vertical $z$ levels : (a) 1 dm above, (b) at, (c) 2 mm below the water/rubber interface, and (d) 2 mm above, (e) at the rubber/steel interface.

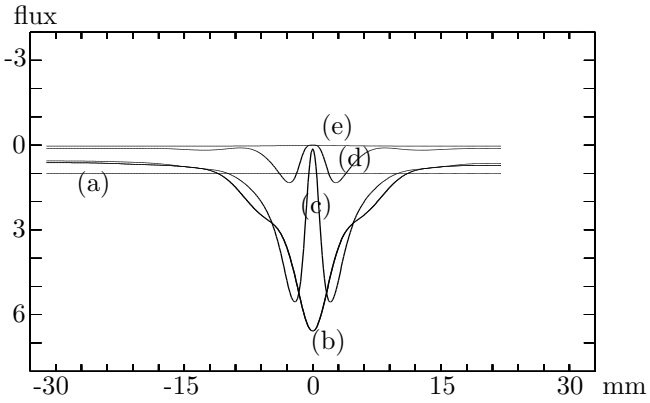


Figure 11: Horizontal distribution of time-averaged vertical flux in the downward (positive $z$) direction at 9 kHz. The spherical scatterer is at the center, with the horizontal axis indicating horizontal distance. Positive and negative distance values are used for the axial and diagonal horizontal directions, respectively, *cf.* Fig. 2. There are five curves, (a)-(e), corresponding to successively increasing depths $z$, as described in the text. The vertical axis shows dimensionless flux values, scaled with the flux (in W/m$^2$) of the incident plane wave.

The specularly reflected wave vanishes at 9 kHz, and 1 dm above the water/rubber interface, the evanescent reflected waves have died out. Hence, it is the laterally constant energy flux of the incident plane wave that is seen in curve (a). Already when the interface is

reached, curve (b), a redistribution of the vertical flux has taken place, with a focusing above the spherical scatterers. The total flux is of course unchanged, since no loss is suffered in the water, as is also realized by an integration over the unit cell with the correct area weighting.

The three remaining curves, (c)-(e), in Fig. 11 show a successively decreasing flux, caused by the loss that is suffered in the rubber layer. At $(x, y) = (0, 0)$, $\mathcal{F}_z$ should vanish at the spherical surface because of the boundary condition and the symmetry. Indeed, curves (c) and (d) exhibit very small values at this point. Some slight numerical inaccuracy can be noted because of a truncation to a finite number of plane and spherical waves. Curve (e) represents the small amount of energy that is transmitted into the steel half-space.

The horizontal components of the time-averaged energy flux vector $\mathcal{F}$ are also of interest. For points in the axial and diagonal directions, the transverse component vanishes for reasons of symmetry but the inward component is shown in Fig. 12. Vanishing values are of course obtained at $(x, y) = (0, 0)$, and also at $x = d/2 = 22$ mm for the axial direction (right end in the figure) and at $x = y = d/\sqrt{2} = 31.1$ mm for the diagonal direction (left end). It can be seen how an inwards horizontal flux appears, pushing energy towards the spherical scatterers, in the vicinity of which it is absorbed. This is consistent with the results at 9 kHz in Fig. 10. An outwards horizontal flux is only noted for the (c) curve, the one for the upper $z$ level of the spheres, and at close distances. Apparently, only part of the incoming energy at the top of a spherical scatterer can be absorbed there. The remaining part is transported away for absorption elsewhere.

The differences between the axial and diagonal directions in Figs. 11 and 12 are small in general, indicating a similar behavior in different horizontal directions around each scatterer. The only clear exceptions are the right and left end parts in Fig. 12, caused by the different distances to lattice points of symmetry in the axial and diagonal directions.

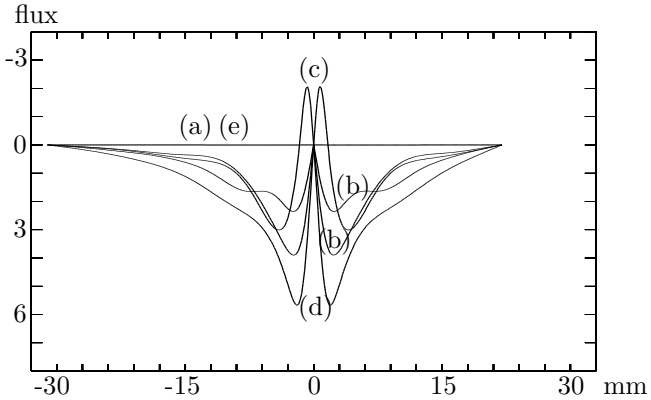


Figure 12: As Fig. 11 but for the time-averaged horizontal flux in the inward direction. The horizontal flux is not continuous across the water/rubber interface, however. Hence, there are two (b) curves in this figure. The lower one, indicating the larger flux, is for the rubber side.

The time-averaged energy flux vector $\mathcal{F}$ can of course be expressed in spherical rather than Cartesian or cylindrical basis vectors. This is perhaps more natural when considering the flux variation along spherical surfaces, as done in Figs. 13 and 14. In these figures, curves (a) and (b) concern the radii 5 and 3 mm, respectively, for a spherical surface centered at one of the spherical scatterers. The horizontal axes indicate the spherical coordinate $\theta$, with the axial azimuthal direction ($\phi = 0^o$) to the right and the diagonal azimuthal direction ($\phi = 45^o$) to the left.

The (a) curve in Fig. 13 shows large inwards radial flux at $r = 5$ mm. This is of course expected from the 9 kHz absorption results of Fig. 10. This flux is fairly constant over the upper hemisphere ($90^o < \theta < 180^o$) and adjacent parts of the lower hemisphere. Directly below a cavity (at $\theta = 0^o$), however, the flux is very small. This has already been observed in connection with the (e) curve in Fig. 11. The radial flux at $r = 3$ mm, corresponding to the surface of the spherical scatterer itself, vanishes of course identically.

The corresponding flux in the negative $\theta$ direction, along the spherical surfaces, is shown in Fig. 14. It is in general positive. Hence, there is a downward component combined with an

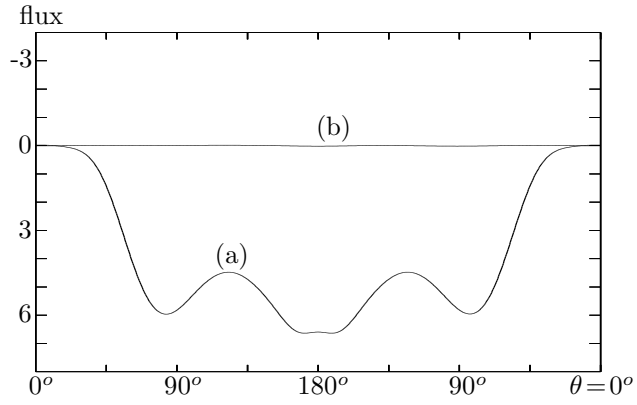


Figure 13: Angular distribution of time-averaged inwards radial flux at 9 kHz around a spherical scatterer. The horizontal axis indicates the spherical coordinate $\theta$, with the axial and diagonal azimuthal directions to the right and left, respectively. The curves (a) and (b) correspond to radial distances of 5 and 3 mm to the center of the scatterer, respectively. As in Figs. 11 and 12, the vertical axis shows dimensionless flux values, scaled with the flux (in $W/m^2$) of the incident plane wave.

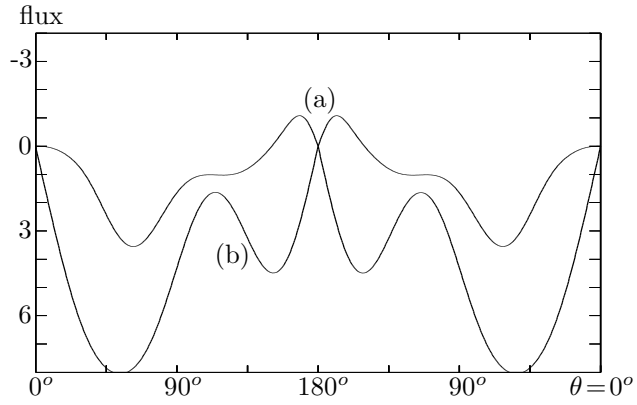


Figure 14: As Fig. 13 but for the time-averaged flux in the negative $\theta$ direction along the spherical surfaces.

outward/inward component in the upper/lower hemisphere. The only exception is the inward flux above the cavity for $r = 5$ mm, the (a) curve.

### C. Different field representations

Two different representations of the field in a particular layer, with periodically distributed spherical scatterers, have been introduced and combined in Secs. II and III. The first is a linear combination of plane waves, each of the type given by Eq. (3) with $\mathbf{g}$ belonging to the reciprocal lattice specified in Eq. (2). This representation was used for the energy flux computations for Figs. 11 and 12. It is appropriate away from the scatterer interface. In the vicinity of this interface, the evanescent waves have not died out and a vast number of plane waves ($\mathbf{g}$ values) would be needed. This is readily realized from Eq. (18).

The second representation involves spherical waves, separated into incoming and outgoing ones. For the scatterer at the origin, for example, these waves are expressed by Eqs. (19) and (16), respectively. This representation was used for the energy flux computations for Figs. 13 and 14. It is appropriate in the vicinity of the chosen scatterer, where a reasonably small number of spherical waves ($lm$ values) is adequate. As an adjacent scatterer is approached, another separation into incoming and outgoing waves would be more appropriate.

The plane-wave representation handles boundary conditions at interfaces between homogeneous layers exactly (via R/T coefficients), whereas the spherical-wave representation handles boundary conditions at a spherical scatterer exactly (via the T-matrix). A large number of components was used in each case to reproduce the lateral variations of the energy flux in Sec. V.B.

In principle, the two field representations are compatible only if many components are included. When total power, or laterally averaged energy flux, is considered, however, good results can actually be obtained with very few field components. The result of Fig. 8, for example, is virtually unchanged if the computations are truncated to include only $Plm = L00$ for the spherical waves. A further truncation to normal beams, only keeping the $\mathbf{g} = \mathbf{0}$ plane waves, produces the result shown in Fig. 15. The reflectivity minima are still there, even if they have become less deep and shifted to somewhat higher frequencies. The single-scattering approximation still has the effect of lowering

the frequency of the reflectivity minimum.

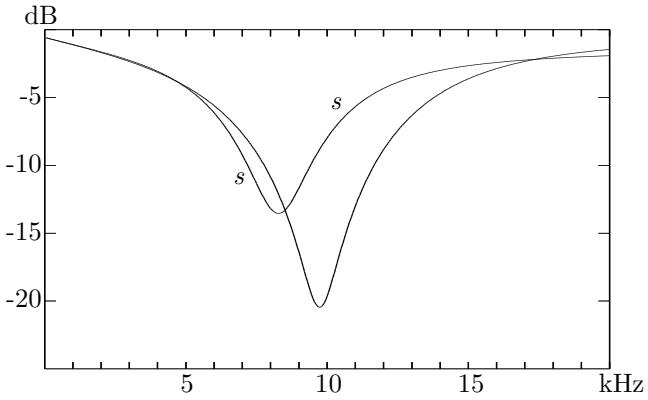


Figure 15: Reflected power for the same case as in Fig. 8, but a truncation to $lm = 00$ and normal beams is invoked.

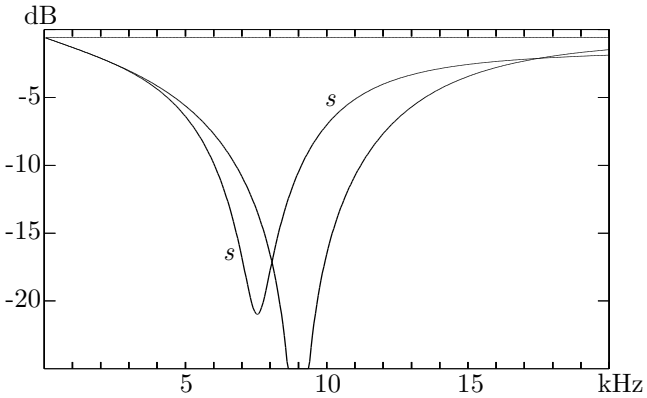


Figure 16: Reflected power as in Figs. 8 and 15. The rubber shear modulus $\mu$ is slightly different, however, determined to achieve zero reflectivity at 9 kHz in the context of the field truncation to $lm = 00$ and normal beams.

The evanescent plane waves are needed to fulfil the boundary conditions at the cavity interfaces, and to produce the lateral variations of the time traces in the middle panel of Fig. 9 and of the energy flux above the water/rubber interface, for example. Nevertheless, a truncation to $Plm = L00$ and normal beams is very useful to understand the mechanism behind the anechoic effect. An important advantage is that the numerical computations can be complemented with theoretical considerations in this way, which is the topic of the next section.

## VI. MECHANISM FOR THE ANECHOIC EFFECT AS ANALYSED WITH TRUNCATED FIELDS

By redoing the winding-integral computations of Sec. V, to obtain vanishing reflected power at 9 kHz for the truncated fields, the results in Fig. 16 are obtained. The appropriate values for shear velocity and absorption of the rubber are now 81.2 m/s and 18.7 dB/wavelength, respectively. The differences between Figs. 8 and 16 are almost negligible.

The echo reduction mechanism, including the effect of multiple scattering, is now discussed within the simplified framework and the example case from Fig. 16 is used. Specifically, *cf.* Sec. V.C, a field representation with the $L00$ term of Eqs. (19) and (16) is used within the rubber layer, and only the normal term $\mathbf{g} = \mathbf{0}$ of Eq. (18) is kept for the boundary-condition match at the interfaces to the normal plane waves in the water and steel half-spaces.

### A. Plane-wave reflection and transmission coefficients

The scatterer interface in the middle of the rubber layer is considered to be at $z = 0$. By restriction to $Plm = L00$, Eqs. (20)-(21) give

$$b' = \Omega b^+ \quad , \quad b^+ = \frac{Ta^0}{1 - \Omega T} \; . \tag{28}$$

Here, and in the following in general, $Plm = L00$ is omitted from the notation. By Eq. (19), the spherical wave that is incident on the sphere at the origin, for example, can thus be written

$$\left(a^0 + b'\right) \, \mathbf{u}_{00}^{0L}(\mathbf{r}) \, = \, \frac{a^0}{1 - \Omega T} \, \mathbf{u}_{00}^{0L}(\mathbf{r}) \; . \tag{29}$$

For the basic case of a plane compressional wave with displacement amplitude unity, $a^0 = -\mathrm{i}\sqrt{4\pi}$ and, by applying Eqs. (13) and (18), Eq. (17) reduces to

$$\mathbf{u}_{sc}(\mathbf{r}) \, = \, \Theta \, \mathrm{e}^{\mathrm{i}k|z|} \cdot \mathrm{sgn}(z) \, \mathbf{e}_z \; , \tag{30}$$

where $k = \omega/\alpha$, $\mathbf{e}_z$ is the unit vector in the $z$ direction, and

$$\Theta = \frac{T}{1 - \Omega T} \, \frac{2\pi}{(kd)^2} \; . \tag{31}$$

Hence, for this basic incident-wave case, the complex amplitudes of the reflected and transmitted waves from the scatterer interface become $\Theta$ and $1 + \Theta$, respectively. The quantity $\Omega$ can be expressed as [26, 27]

$$\Omega = \sum_{\mathbf{R} \neq \mathbf{0}} \mathrm{h}_0^+(k|\mathbf{R}|) \; . \tag{32}$$

The sum must be interpreted in a generalized sense, for example as a limit for complex $k$ with positive $\mathrm{Im}(k)$ decreasing to zero. Vanishing normal traction at $r = a = 3$ mm is obtained with

$$T = -\frac{ka\,\mathrm{j}_0(ka) + 4\,(\beta^2/\alpha^2)\,\mathrm{j}_0'(ka)}{ka\,\mathrm{h}_0^+(ka) + 4\,(\beta^2/\alpha^2)\,(\mathrm{h}_0^+)'(ka)} \; . \tag{33}$$

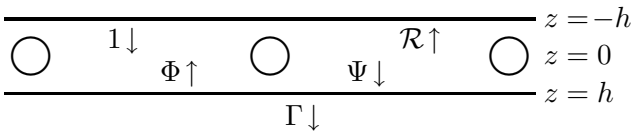


Figure 17: The rubber layer from Fig. 1 is shown, with thickness $2h$ and the scatterer interface at $z = 0$ in the middle. Hence, the water and steel half-spaces appear in $z < -h$ and $z > h$, respectively. Notation for some normal plane-wave complex displacement amplitudes is also included. These amplitudes are evaluated at $z = 0$, except $\Gamma$ which is evaluated at $z = h$ (the rubber/steel interface).

Including the rubber/steel interface at the distance $h = 5$ mm as illustrated in Fig. 17, with displacement reflection coefficient $\sigma$, Eqs. (7)-(8), with $E = \exp(\mathrm{i}\omega h/\alpha)$, $\mathcal{R}_{B1} = \mathcal{R}_{A1} = \Theta$, $\mathcal{T}_{B1} = \mathcal{T}_{A1} = 1 + \Theta$, $\mathcal{R}_{B2} = E^2\sigma$, and $\mathcal{T}_{B2} = (1 - \sigma)E$, provide the relations

$$\mathcal{R} = \mathcal{R}_B \;=\; \frac{\Theta(1 + 2E^2\sigma) + E^2\sigma}{1 - E^2\sigma\Theta} \tag{34}$$

$$\Gamma = \mathcal{T}_B \;=\; \frac{E(1 - \sigma)(1 + \Theta)}{1 - E^2\sigma\Theta} \tag{35}$$

for the reflection- and transmission-coefficients $\mathcal{R}$ and $\Gamma$, respectively. The water/rubber interface, *cf.* Fig. 1, can be ignored in the present context with normal beams only, since the density and compressional-wave velocity are assumed to be the same in the water and in the rubber. The complex displacement amplitude of the incident wave is assumed to be unity at the scatterer interface.

The wave field between the scatterer and rubber/steel interfaces can be described by complex displacement amplitudes $\Phi$ and $\Psi$ of up- and down-going waves, respectively, as evaluated at the scatterer interface. One verifies readily that

$$\Phi \;=\; \frac{\mathcal{R} - \Theta}{1 + \Theta} \;=\; \frac{E^2\sigma(1 + \Theta)}{1 - E^2\sigma\Theta} \tag{36}$$

$$\Psi \;=\; (1 + \Theta) + \Phi\Theta \;=\; \frac{1 + \Theta}{1 - E^2\sigma\Theta} \tag{37}$$

The magnitudes of $\mathcal{R}$, $\Theta$, $\Phi$, $\Psi$, $\Gamma$ are plotted as functions of frequency in the upper panel of Fig. 18, for the example case with $\mathcal{R} = 0$ at 9 kHz. Of course, the $|\mathcal{R}|$ curve is merely a dB version of a curve from Fig. 16. Corresponding results within the single-scattering approximation, *i.e.*, with $\Omega$ set to zero, are shown in the lower panel of Fig. 18. In particular, the minimum of $|\mathcal{R}|$ is shifted from 9 kHz to about 7.5 kHz, as has already been seen in Fig. 16.

Corresponding results for an elastic rubber material, with vanishing shear-wave absorption, are shown in Fig. 19. Large values of $|\mathcal{R}|$ are obtained at all frequencies. Instead of a minimum, a maximum with almost total reflection ($|\mathcal{R}| \approx 1.0$) appears at about 10.0 kHz in the upper panel. Virtually no energy is transmitted through the scatterer interface at that frequency. The existence of transmission band gaps for phononic crystals is well known, [28, 29] and periodic frequency selective surfaces (FSS) constitute an active research area in electromagnetics. [30]

Single-scattering results for the elastic rubber are shown in the lower panel of Fig. 19. Unphysical results are obtained, with $|\Theta|$ as well as

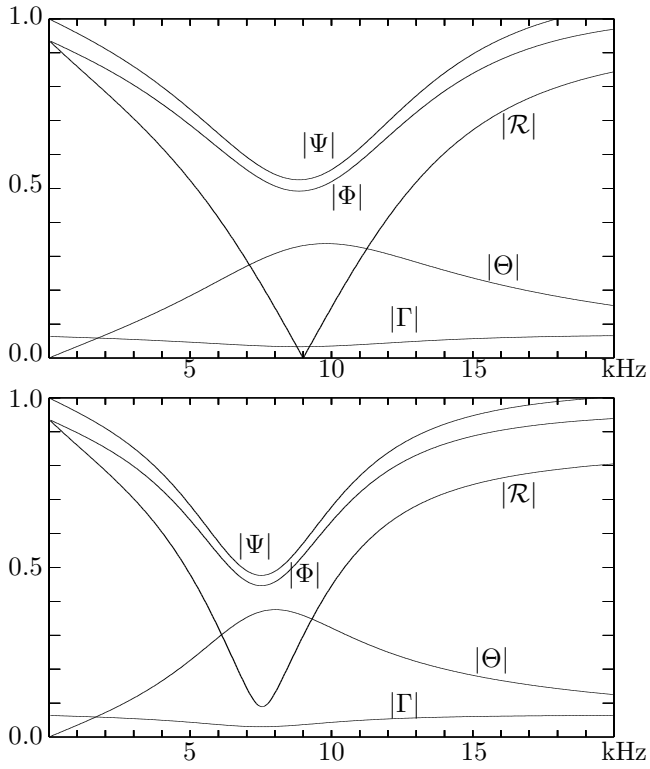


Figure 18: The magnitudes of the quantities from Fig. 17, and $|\Theta|$ as well, are plotted as functions of frequency for the parameter values of the example case. The lower panel concerns the single-scattering approximation, with $\Omega$ set to zero.

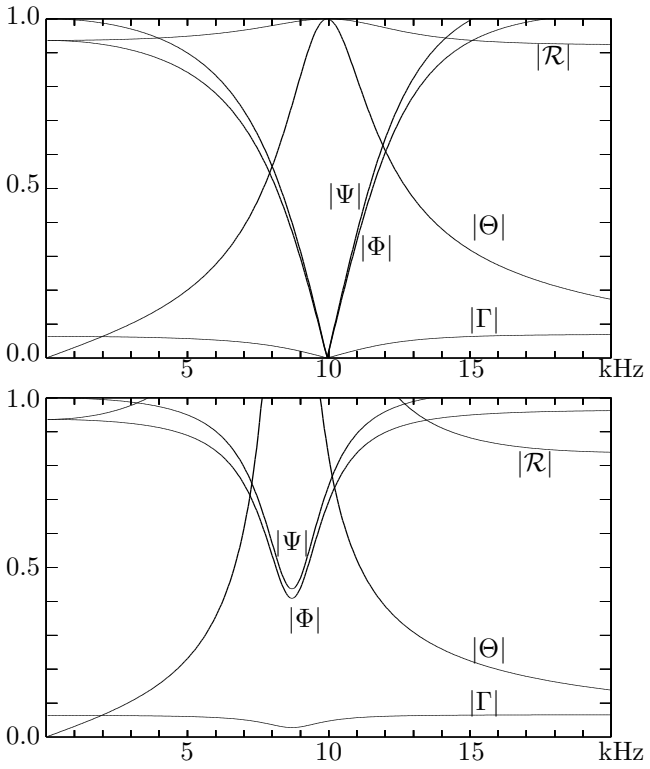


Figure 19: As Fig. 18 but for an elastic rubber material (the shear-wave absorption in the rubber is set to zero). Again, the lower panel concerns the single-scattering approximation.

$|\mathcal{R}|$ exceeding unity. As clarified in Sec. VI.D, see Eq. (55) below, multiple-scattering effects are essential to avoid such inconsistencies.

A common feature in Figs. 18 and 19 is a maximum of $|\Theta|$. At low frequency, the inclusions are small in comparison to the wavelength and $\Theta$ is small as well. The maxima for $|\Theta|$ in the lower panels correspond to maxima for $|T|/\omega^2$, *cf.* Eq. (31), a resonance effect which is further discussed in Sec. VI.C.

### B. Expanding the Riccati reverberation operator

The reverberation operator $[\mathbf{I}-\mathcal{R}_{A1}\cdot\mathcal{R}_{B2}]^{-1}$ appearing in Eq. (7) can be expanded in a geometric series [18] and individual wavefield components can be isolated. Eq. (7) becomes

$$\mathcal{R}_B \;=\; \mathcal{R}_{B1} \,+\, \mathcal{T}_{A1}\cdot\mathcal{R}_{B2}\cdot\mathcal{T}_{B1} \,+\, \mathcal{T}_{A1}\cdot\mathcal{R}_{B2}\cdot\mathcal{R}_{A1}\cdot\mathcal{R}_{B2}\cdot\mathcal{T}_{B1} \,+\, \ldots \quad (38)$$

Including vertically travelling plane compressional waves only, Eq. (38) is illustrated in Fig. 20 for the first three terms.

As applied to $\mathcal{R} = \mathcal{R}_B$ of Eq. (34), with $E = \exp(\mathrm{i}\omega h/\alpha)$, $\mathcal{R}_{B1} = \mathcal{R}_{A1} = \Theta$, $\mathcal{T}_{B1} = \mathcal{T}_{A1} = 1 + \Theta$, $\mathcal{R}_{B2} = E^2\sigma$, and $\mathcal{T}_{B2} = (1-\sigma)E$, the basic case of Fig. 16 can be recovered. The results are shown in Fig. 21. Of course, the one-term result is merely a dB version of the $|\Theta|$ curve from the upper panel of Fig. 18. Already the two-term result, with no more than one wave interaction with the rubber/steel interface, reproduces the anechoic effect rather well. Including the first multiple, the three-term case, the result is very similar to that in Fig. 16. The four-term result provides a further refinement, and the anechoic effect can be understood in terms of a destructive interference among the waves appearing in the right-hand

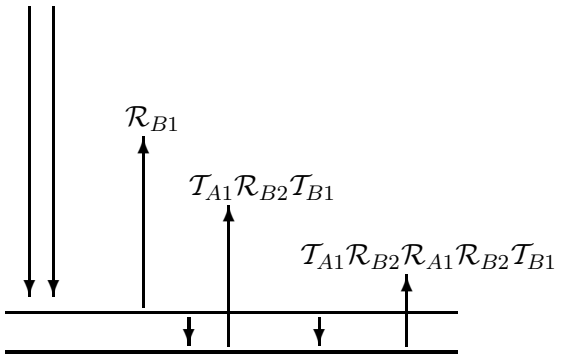


Figure 20: Reverberation-operator approximations with one, two, and three terms according to Eq. (38) are illustrated with the corresponding (multiply) reflected waves.

side of Eq. (38).

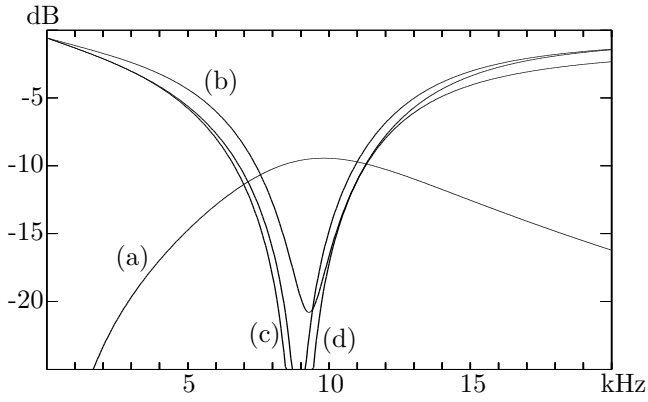


Figure 21: Reverberation-operator approximations with (a) one, (b) two, (c) three, and (d) four terms according to Eq. (38) are used to recover the result of Fig. 16.

### C. Requirements for anechoism

The fraction of the incident energy that is lost by anelastic absorption is computed as

$$1 - |\mathcal{R}|^2 - \frac{\mathrm{Z}_{steel}}{\mathrm{Z}_{rubber}} |\Gamma|^2 \,, \qquad (39)$$

where $\mathrm{Z}_{steel}$ and $\mathrm{Z}_{rubber}$ are the characteristic impedances [31] of the steel and the rubber, respectively. Multiplication with $d^2/\pi a^2$ provides the effective normalized absorption cross-section per cavity, which is shown by curve (a) of Fig. 22. The results are similar to those in Fig. 10, for the example of Sec. V with all field components included.

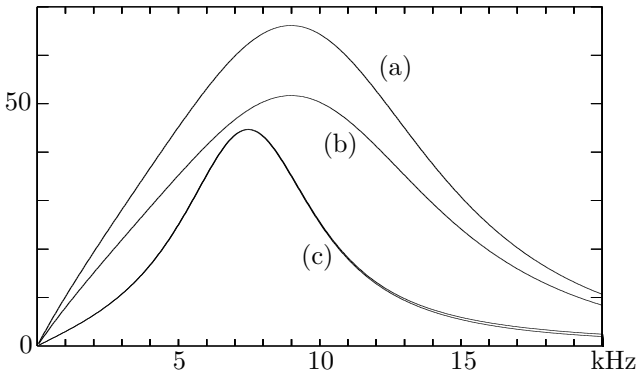


Figure 22: For the example case of Sec. VI, curve (a) shows the frequency dependence of the effective normalized absorption cross-section per cavity in the lattice. The contribution from anelastic absorption within 2 mm of a cavity is indicated by curve (b). The normalized absorption cross-section for a single spherical cavity of radius 3 mm embedded in rubber is shown by (c). Two almost coinciding (c) curves are shown, the lower one includes only the $lm$ = 00 contribution.

At a frequency for which $\mathcal{R} = 0$, it follows from Eqs. (34)-(37) that

$$\Theta = -\frac{E^2\sigma}{1+2E^2\sigma} \qquad (40)$$

$$\Gamma = \frac{(1-\sigma)}{1+E^2\sigma} \qquad (41)$$

$$\Phi = \frac{E^2\sigma}{1+E^2\sigma} \qquad (42)$$

$$\Psi = \frac{1}{1+E^2\sigma} \,. \qquad (43)$$

It can be noted that $\Phi + \Psi = 1$ here, and the expression (39) for the fraction of the incident energy that is absorbed reduces to

$$1 - \frac{1-\sigma^2}{|1+E^2\sigma|^2} \,. \qquad (44)$$

For the example case at 9 kHz, with $\mathcal{R} = 0$, $\sigma$ = 0.9364 and $E = 0.9818 + 0.1899\mathrm{i}$. It follows,

for example, that only 0.4 % of the incident energy is transmitted through the steel half-space. The remaining 96.6 % are thus absorbed. Furthermore, $\Theta$ = -0.3285 - 0.0437i at 9 kHz. The cancellation for $\mathcal{R}_B$ that is expressed by the reverberation series (38) takes the form

$$\begin{aligned} \mathcal{R}_B &= \Theta + (1+\Theta)^2 E^2 \sigma + \\ &\quad (1+\Theta)^2 (E^2\sigma)^2 \Theta + \ldots \qquad (45) \\ &= (-0.3285 - 0.0437\mathrm{i}) + \\ &\quad (0.4106 + 0.1057\mathrm{i}) + \\ &\quad (-0.0948 - 0.0913\mathrm{i}) + \ldots . \qquad (46) \end{aligned}$$

It remains to understand how the particular value $\Theta$ = -0.3285 - 0.0437i at 9 kHz can be achieved, in terms of scattering from the spherical cavities. Normalized cross-section values as large as 66.0, as seen at 9 kHz in curve (a) of Fig. 22, indicate the necessity of a strong resonance effect.

The normalized absorption cross-section for a single spherical cavity of radius 3 mm is shown by curve (c) of Fig. 22, as a function of frequency. The single cavity is embedded in rubber with the same parameters as in the example case. Of course, the absorption loss takes place in the surrounding rubber material. Formulas for computing absorption, as well as scattering, cross-sections in this context are derived in Appendix C. As compared to curve (a), the resonance frequency is shifted from 9.0 kHz (where the value is 35.0) to 7.5 kHz, where the maximum 44.7 appears. The differences are mainly caused by multiple scattering among the cavities in the lattice. They are discussed and quantified in Secs. VI.D and VI.E below.

There are in fact two (c) curves in Fig. 22. The lower one only includes the $lm = 00$ contribution, which dominates and the two curves can hardly be distinguished.

With shear-wave absorption in the surrounding rubber material, the resonance appears much more clearly in the absorption cross-section than in the scattering cross-section. This is realized by comparing to curve (a) in Fig. 23, with values less than 8.0 at all frequencies. Curve (a) in Fig. 23 is completely dominated by its $lm = 00$ contribution (see Eq. (97) in Appendix C).

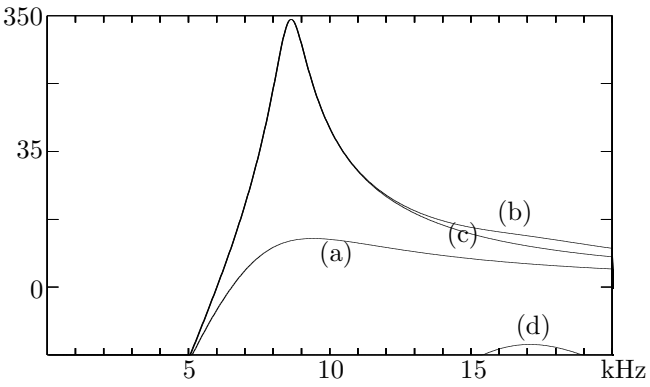


Figure 23: Normalized scattering cross-sections, as functions of frequency, for a spherical cavity of radius 3 mm in rubber. The incident wave is a plane compressional wave, as usual. The scale on the vertical axis is logarithmic. Curve (a) concerns the rubber of the example case with shear absorption and only the compressional-wave part remains at large distances. Curves (b)-(d) concern the elastic case. Curve (b), for the total cross-section, is the sum of a compressional-wave part (c) and an almost negligible shear-wave part (d).

The remaining curves in Fig. 23 concern the elastic case without rubber shear-wave absorption. At 8.6 kHz, the single cavity appears to be much larger,[33] with a normalized cross-section that is almost 330.0. This value exceeds $d^2/\pi a^2$ = 68.5 by a factor of almost five, which is of course related to the unphysical appearance of $|\mathcal{R}|$ values exceeding 1.0 in the lower panel of Fig. 19, when multiple scattering is ignored.

The shear-wave contributions to the scattering cross-section are small. Below about 12 kHz, they are negligible in comparison to the compressional-wave contributions, which are again completely dominated by the $lm$ = 00 term. In fact, an evacuated spherical inclusion in an elastic solid with a reasonably small shear-wave velocity has a monopole scattering resonance when the circumference equals two shear wavelengths in the solid. This is the classical Meyer *et al.* [6] resonance. A generalization can be found in equation (19) of Ref. [3], see

also equation (3) of Ref. [32]. It is the radial displacement amplitude at the sphere surface that has its maximum at the corresponding frequency (8.611 kHz for the elastic case considered here). The $lm = 00$ contribution to the scattering cross-section is governed by $|T|^2/\omega^2$, where $T$ is given by Eq. (33), and this quantity has its maximum at a slightly different frequency (8.637 kHz here). The maximum of $|T|$ itself appears at yet another frequency (8.664 kHz). It is always unity in the elastic case, for a vanishing imaginary part, but when significant shear-wave absorption is introduced, $|T|$ is reduced significantly (*cf.* Fig. 23). Clearly, [3] this classical resonance of a bubble in a solid is of decisive importance for the anechoic effect studied here.

### D. An energy relation valid for the truncated fields

The effective normalized absorption cross-section per cavity can be expressed in another way, where the effects of multiple scattering are separated in a modulating factor. Specifically, the following energy relation is valid when $k = \omega/\alpha < 2\pi/d$:

$$\frac{d^2}{\pi a^2}\left(1 - |\mathcal{R}|^2 - \frac{\mathrm{Z}_{steel}}{\mathrm{Z}_{rubber}}|\Gamma|^2\right) = \left|\frac{1+\Phi}{1-\Omega T}\right|^2 \frac{4|T|^2[-1-\mathrm{Re}(1/T)]}{(ka)^2} \ . \quad (47)$$

In order to prove (47), Eqs. (34)-(35) and the relation $\mathrm{Z}_{steel}/\mathrm{Z}_{rubber} = (1+\sigma)/(1-\sigma)$ are first used to rewrite the left-hand side as

$$\frac{d^2}{\pi a^2|1-E^2\sigma\Theta|^2}\left[\,|1-E^2\sigma\Theta|^2 - |\Theta+E^2\sigma+2E^2\sigma\Theta|^2 - (1-\sigma^2)|1+\Theta|^2\,\right] \ . \quad (48)$$

Using Eqs. (31) and (36), the right-hand side is subsequently rewritten as

$$\frac{|1+E^2\sigma|^2}{|1-E^2\sigma\Theta|^2}\left(\frac{kd^2}{\pi a}\right)^2|\Theta|^2\left[-1-\mathrm{Re}\left(\frac{1}{T}\right)\right] \ . \quad (49)$$

In general, $\Omega$ as given by Eq. (32) must be computed numerically. [19] When $k$ is real with $kd < 2\pi$, however, a wave-theoretic argument can be used [34] to obtain an explicit expression for the real part of $\Omega$:

$$\mathrm{Re}(\Omega) = \frac{2\pi}{(kd)^2} - 1 \ . \quad (50)$$

Applying Eq. (50) together with Eq. (31), the expression (49) takes the form

$$-\frac{2d^2|1+E^2\sigma|^2[|\Theta|^2+\mathrm{Re}\,\Theta]}{\pi a^2|1-E^2\sigma\Theta|^2} \ . \quad (51)$$

It follows that Eq. (47) boils down to the relation

$$|1-E^2\sigma\Theta|^2 - |\Theta+E^2\sigma+2E^2\sigma\Theta|^2 - (1-\sigma^2)|1+\Theta|^2 = -2|1+E^2\sigma|^2\left[|\Theta|^2+\mathrm{Re}\,\Theta\right] \ . \quad (52)$$

Assuming as before that $|E| = 1$ and that $\sigma$ is real, Eq. (52) is easily verified, which concludes the proof.

Equation (33) for $T$ can be rewritten as

$$\frac{1}{T} = -1 - \mathrm{i}\frac{ka\,\mathrm{y}_0(ka) + 4\,(\beta^2/\alpha^2)\,\mathrm{y}_0'(ka)}{ka\,\mathrm{j}_0(ka) + 4\,(\beta^2/\alpha^2)\,\mathrm{j}_0'(ka)} \ . \quad (53)$$

For real $\alpha$ and $ka$, it follows by applying a Wronskian expression that

$$-1 - \mathrm{Re}(1/T) = \frac{4\,\mathrm{Im}(-\beta^2)}{\alpha^2\,ka\,|ka\,j_0(ka)+4\,(\beta^2/\alpha^2)\,j_0'(ka)|^2} \geq 0 \ . \quad (54)$$

Hence, both sides of Eq. (47) are nonnegative. For the particular case when the steel is replaced by rubber, corresponding to $\mathrm{Z}_{steel} = \mathrm{Z}_{rubber}$, $\sigma = 0$ and it follows from Eqs. (47) and (54) that

$$|\Theta|^2 + |1+\Theta|^2 \leq 1 \ . \quad (55)$$

As can be seen from Eq. (31), with small $d$ and temporarily taking $\Omega = 0$ for a single-scattering approximation, multiple-scattering effects are crucial for this physically reasonable bound on $\Theta$. This has already been noted in connection with Fig. 19.

### E. Absorption of energy close to the spheres

The right-hand side of Eq. (47) has an interesting physical interpretation, that links the

loss in the rubber layer to the absorption cross-section for an isolated spherical cavity. The wave field in the vicinity of the sphere at the origin, for example, can be expressed as

$$(1+\Phi)\,\frac{a^0}{1-\Omega T}\,\left(\,\mathbf{u}_{00}^{0L}(\mathbf{r})\,+\,T\,\mathbf{u}_{00}^{+L}(\mathbf{r})\,\right)\,, \tag{56}$$

where $a^0 = -\mathrm{i}\sqrt{4\pi}$ is the expansion coefficient for a plane compressional wave of displacement amplitude unity. This follows from the definition of $\Phi$, *cf.* Fig. 17, and Eq. (29) together with Eq. (20). The factor $4|T|^2\,[-1-\mathrm{Re}(1/T)]\,/(ka)^2$ in Eq. (47) equals the naturally normalized total power loss by anelastic absorption for the basic spherical wave field

$$\begin{aligned}\mathbf{u}(\mathbf{r}) &= a^0\,\left(\,\mathbf{u}_{00}^{0L}(\mathbf{r})\,+\,T\,\mathbf{u}_{00}^{+L}(\mathbf{r})\,\right)\\ &= -\mathrm{i}\,\left(\,\mathrm{j}_0'(kr)\,+\,T\,(\mathrm{h}_0^+)'(kr)\right)\cdot\mathbf{e}_r\,.\end{aligned} \tag{57}$$

This identification follows from Eq. (97) of Appendix C. The natural normalization is made with the cross-section power for an incident plane wave with displacement amplitude unity.

For the example case, the factor $4|T|^2\,[-1-\mathrm{Re}(1/T)]\,/(ka)^2$ for Eq. (47) has already been plotted as the lower (c) curve in Fig. 22. The modulating factor $|(1+\Phi)/(1-\Omega T)|^2$ is shown in Fig. 24, along with its two contributing partial factors $|(1+\Phi)|^2$ and $|1-\Omega T|^{-2}$ taking effects of multiple scattering into account. As has already been noted by comparing the (a) and (c) curves in Fig. 22, the modulation causes loss magnification and the loss peak is shifted to the frequency 9 kHz.

A simple factorization of the absorption loss, as given by Eq. (47), does not seem to be valid when all plane-wave components are retained. Indeed, the rubber layer does not extend to infinity in the $z$ direction and the small loss contributions for large $r$ are not relevant. With the given interpretation of its right-hand side, the attractive factorization of Eq. (47) seems to be a fortuitous consequence of the restriction to truncated fields.

For the wave field of Eq. (57), with cavity radius and parameters for the surrounding solid

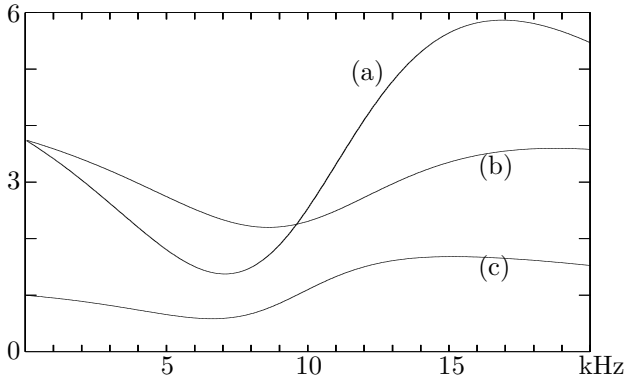


Figure 24: For the parameter values of the example case, curve (a) shows the modulating factor for the effective normalized absorption cross-section per cavity in Eq. (47). This factor is the product of $|(1+\Phi)|^2$ and $|1-\Omega T|^{-2}$, which are shown by curves (b) and (c), respectively.

as in the example case, the time-averaged strain power density at 9 kHz is plotted as a function of radius in Fig. 25. An integration over the centered sphere with radius $r$ provides $\mathcal{P}(r)$, the amount of loss suffered within this sphere (see Appendix C). The function $\mathcal{P}(r)$ is also plotted in Fig. 25, as normalized with the total loss given by $\mathcal{P}(+\infty) = \lim_{r\to\infty}\mathcal{P}(r)$. It can be noted that about 78 % of the loss takes place within $r = 5$ mm, which is a particular case already considered in curve (b) of Fig. 22.

For the particular wave field according to Eq. (57), the dominant contribution to the strain power density for $kr << 1$ comes from the scattered field. Using Eqs. (101)-(102) of Appendix C, some calculation with spherical Hankel functions provides the expression

$$\frac{6\omega|T|^2}{(kr)^4 r^2}\,\mathrm{Im}(-\mu) \tag{58}$$

for this dominant contribution, where $\mu$ is the complex shear modulus. The loss appears because of deviatoric stress and strain in the angular directions $\theta$,$\phi$, that become significant at small $r$.

For a wave field given by (57), it might have been expected that the strain power density

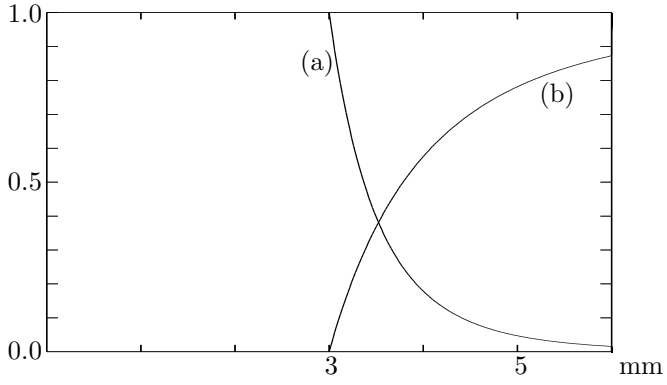


Figure 25: (a) For the example case with, in particular, $a = 3$ mm, the strain power density for the wave field given by Eq. (57) is shown as a function of radius $r$. It is normalized with its maximum value, which appears at $r = a$. The frequency is 9 kHz. (b) Fractions of power loss by anelastic absorption that take place within spheres of radius $r$, centered at the origin.

could be expressed in terms of the modulus $\rho\alpha^2$ and the T-matrix coefficient $T$, without any need to involve the shear modulus $\mu$ explicitly. This is not the case, however, since the corresponding stress tensor components depend on $\mu$, as discussed by Blake. [35] For example,

$$\tau^{rr} = \rho\alpha^2 \left( \frac{\partial u}{\partial r} + \frac{2u}{r} \right) - 4\mu \frac{u}{r} \qquad (59)$$

and a restoring stress $-4\mu u/r$ can be identified, which is absent in a fluid. Regimes of stiffness control and inertia control appear for the specific acoustic impedance. [35]

## VII. CONCLUDING REMARKS

The echo reduction by Alberich anechoic coatings can be studied by semi-analytical wave theory, as reviewed in Secs. II and III. A fundamental property of scatterers in a periodic planar lattice is to redistribute incoming plane-wave energy to reflected beams, not only in the specular direction but in a discrete set of other directions. A coating that scatters incoming energy in nonspecular directions could be of interest, even if the energy is not absorbed. The nonspecular beams are evanescent at low frequency, however, and for the examples in Sec. IV, only a small amount of energy is linked off in nonspecular directions.

By choosing the coating impedance appropriately, the normal-incidence reflection from an interface between two arbitrary half-spaces can be eliminated by a homogeneous quarter-wavelength coating. [8] As seen in Sec. V, introduction of spherical cavities allows reflection elimination for a coating with a thickness that is only 6 % of the wavelength. As quantified by computations of absorption cross-sections and energy flux, most of the absorption loss is suffered in the vicinity of the cavities. It is quite possible to achieve vanishing reflectivity with still thinner coatings, in relation to the wavelength, but the required shear velocity and shear absorption for the rubber are decreased and increased, respectively. In the end, the limits for realistic rubber materials are reached. Continuing with the example of Sec. V, anechoism at 6 rather than 9 kHz is obtained at 62.6 rather than 83.6 m/s and 21.1 rather than 14.3 dB/wavelength for the rubber shear parameters.

The nonspecular plane waves are important for many of the pulse computation results in Secs. IV (obliquely directed plane waves) and V (evanescent waves at the water/rubber interface). For the power versus frequency results, however, truncation of these waves is useful to obtain the following simplified explanation of the mechanism for the anechoic effect at 9 kHz in Fig. 16 (Sec. VI):

A single cavity of radius $a = 3$ mm has a monopole ($Plm = L00$ in Eq. (16)) resonance[6,3,32] at about 8.6 kHz in the rubber material considered. A small rubber shear velocity is needed to position this Meyer *et al.* resonance[6] at a low frequency. If the rubber were elastic, a plane array of cavities in a quadratic lattice with period $d = 44$ mm would be capable of producing almost total reflection at this frequency for a normally incident plane compressional wave. Multiple scattering among the spherical cavities must be taken into account here, in order to obtain physically reasonable reflection

coefficient values. (The normalized scattering cross-section for a single cavity is about 330.0 at 8.6 kHz, which is much larger than the ratio $d^2/\pi a^2 = 68.5$ between the unit cell and geometrical cross-section areas.) Including the shear-wave absorption, most of the resonance scattering energy disappears by viscoelastic loss processes, but an appropriate amount remains to enable destructive interference among upgoing specular compressional waves from the scatterer and rubber/steel interfaces.

The wavelength of compressional waves at 9 kHz is 164 mm, and the phase changes of the compressional waves when passing through the 10 mm thick rubber plate can be neglected in a simplified analysis. Vanishing reflectivity at 9 kHz would correspond to $\mathcal{R}_B = 0$ from Eq. (7) with $\mathcal{R}_{B1} = \mathcal{R}_{A1} = \Theta$, $\mathcal{T}_{B1} = \mathcal{T}_{A1} = 1 + \Theta$, and $\mathcal{R}_{B2} = 0.94$ (the reflection coefficient at the rubber/steel interface). The equation that is obtained is

$$0 = \Theta + \frac{0.94(1+\Theta)^2}{1 - 0.94\Theta} \ . \qquad (60)$$

It is solved by $\Theta$ = -0.326, which is very close to $\Theta$ = -0.3285 - 0.0437 i that was obtained in Sec. VI.C when phase changes of the compressional wave were included. The main cancellation of the direct reflection $\Theta$ from the scatterer interface is produced already by the first-order interaction with the steel given by $0.94(1+\Theta)^2$, *cf.* Eq. (38).

With monopole scattering resulting in equal amplitudes in the upward and downward directions, as expressed by Eq. (30), a cancellation mechanism of the type described is the only way to achieve anechoism. As stated in Ref. [10], the coating and the underlying structure must be considered together. Extinction of the incident wave already before interaction with the steel, for example, would require cancellation with a downwards scattered wave that would entail an undesired and uncancelled scattered wave in the upward direction.

Energy is lost mainly by absorption of spherically symmetric compressional waves close to the spherical cavities. A large rubber shear-wave absorption is effective in producing this loss. The amount of loss that is suffered is related to the absorption cross-section of an isolated cavity, as modulated according to the complex amplitudes of the insonifying waves, including multiply scattered ones. Within the framework of truncated wave fields, including only vertically travelling plane waves and spherical waves of $Plm = L00$ type, this relation can be expressed as an exact factorization, Eq. (47). The effects of multiple scattering are isolated, and the single-scattering approximation gives rise to clearly noticeable errors in the examples shown.

A coating useful in practice has to provide significant echo reduction within a broad frequency interval. The theoretical winding-number method of Sec. V, to achieve vanishing reflectivity at a particular frequency, is not adequate for this objective. Global optimization techniques, such as genetic or differential evolution algorithms, are better adapted to design such coatings. [36] The present semi-analytical technique allows fast calculations, which is important in connection with coating design. It is appropriate to use coatings with more than one scatterer interface. Different "local" periods can be allowed for the different scatterer interfaces, as long as there is an overall period $d$, which is a multiple of each of the local ones. [36] Several other extensions of the theory reviewed in Secs. II and III appear possible. Nonspherical scatterers could be allowed by incorporating existing T-matrix routines for such bodies, [37] and point-source results could be synthesized by wavenumber integration.

## APPENDIX A: CONDITIONS FOR VERTICAL ENERGY FLUX WITHOUT CROSS-TERMS

The vertical component $\mathcal{F}_z(\mathbf{r})$ of the time-averaged energy flux vector $\mathcal{F}(\mathbf{r})$ can be expressed as [38]

$$\mathcal{F}_z = \frac{\omega}{2} \mathrm{Im} \left( \tau_{xz} u_x^* + \tau_{yz} u_y^* + \tau_{zz} u_z^* \right) \ , \qquad (61)$$

in terms of the indicated components of the

complex displacement amplitude vector $\mathbf{u}(\mathbf{r})$ and stress amplitude tensor $\tau(\mathbf{r})$. A time dependence according to $\exp(-\mathrm{i}\omega t)$ is understood, and the complex conjugate is denoted by an asterix.

The expression of Eq. (61) is quadratic. Specialization is now made to the particular case of a wave field given by a linear combination of plane waves of different horizontal wavenumbers $\mathbf{k}_{||}+\mathbf{g}$ with $\mathbf{g}$ according to Eq. (2), polarizations $j$=1,2,3, and vertical directions $s$=+,− according to

$$\mathbf{u}(\mathbf{r}) \;=\; \sum_{\mathbf{g}js} A_{\mathbf{g}js}\, \exp(\mathrm{i}\,\mathbf{K}^s_{\mathbf{g}j}\cdot\mathbf{r})\cdot\mathbf{e}_j\ . \qquad (62)$$

The polarization vectors $\mathbf{e}_j$ and vertical wavenumbers $\mathbf{K}^s_{\mathbf{g}j}$ have been defined in Eqs. (3)-(5). When Eq. (62) is inserted into Eq. (61), terms involving $|A_{\mathbf{g}js}|^2$ appear, but cross-terms involving $A_{\mathbf{g}js}\,A^*_{\mathbf{g}'j's'}$ for $\mathbf{g}js\neq\mathbf{g}'j's'$ appear as well. Without loss of generality, $z$ is put to zero for simplicity.

Concerning the terms with $\mathbf{g}=\mathbf{g}'$, formulas (7.19)-(7.27) and (7.49)-(7.55) of Ref. [9] can directly be utilized. For each particular $\mathbf{g}$, one obtains a P-SV contribution

$$\begin{aligned}
&\rho|\alpha|^2\ \big(\gamma^*-(2\beta k/\omega)^2\mathrm{Re}(\gamma)\big)\cdot\\
&\qquad\big(|A_{\mathbf{g}1+}|^2-|A_{\mathbf{g}1-}|^2\big)\ +\\
&\rho|\alpha|^2\ \big((2\beta k/\omega)^2\mathrm{Im}(\gamma)-\mathrm{i}\gamma^*\big)\cdot\\
&\qquad 2\,\mathrm{Im}\left(A_{\mathbf{g}1+}\,A^*_{\mathbf{g}1-}\right)\ +\\
&\rho|\beta|^2\ \big(\nu^*-(2\beta k/\omega)^2\mathrm{Re}(\nu)\big)\cdot\\
&\qquad\big(|A_{\mathbf{g}2+}|^2-|A_{\mathbf{g}2-}|^2\big)\ -\\
&\rho|\beta|^2\ \big((2\beta k/\omega)^2\mathrm{Im}(\nu)-\mathrm{i}\nu^*\big)\cdot\\
&\qquad 2\,\mathrm{Im}\left(A_{\mathbf{g}2+}\,A^*_{\mathbf{g}2-}\right)\ -\\
&\quad 4\rho(\beta/\omega)^2 k\,\mathrm{Re}\,[\,\alpha\beta^*\gamma\nu^*\\
&\quad (A_{\mathbf{g}1+}-A_{\mathbf{g}1-})(A_{\mathbf{g}2+}+A_{\mathbf{g}2-})^*]-\\
&\quad 2\rho(\beta/\omega)^2 k(k^2+\nu^2)\,\mathrm{Re}\,[\,\alpha\beta^*\\
&\quad (A_{\mathbf{g}1+}+A_{\mathbf{g}1-})(A_{\mathbf{g}2+}-A_{\mathbf{g}2-})^*] \qquad (63)
\end{aligned}$$

to $\tau_{xz}u^*_x+\tau_{zz}u^*_z$, and an SH contribution

$$\begin{aligned}
&-\rho\beta^2\nu\,\big(\,|A_{\mathbf{g}3+}|^2-|A_{\mathbf{g}3-}|^2+\\
&\qquad 2\mathrm{i}\,\mathrm{Im}(A_{\mathbf{g}3+}\,A^*_{\mathbf{g}3-})\,\big) \qquad (64)
\end{aligned}$$

to $\tau_{yz}u^*_y$. For convenience, the additional notation

$$\begin{aligned}
k &= |\mathbf{k}_{||}+\mathbf{g}| && (65)\\
\gamma &= -\mathrm{i}\,K^+_{\mathbf{g}1z} && (66)\\
\nu &= -\mathrm{i}\,K^+_{\mathbf{g}2z}=-\mathrm{i}\,K^+_{\mathbf{g}3z} && (67)
\end{aligned}$$

has been introduced here. In addition, the horizontal coordinates have been rotated for the particular $\mathbf{k}_{||}+\mathbf{g}$ to align the SH displacement with the $y$ axis.

Assuming that $\beta$ is real, the P-SV cross-term contribution to $\mathcal{F}_z$ disappears, as seen from Eq. (61) and the last two terms of (63). The P ($j=1$), SV ($j=2$), SH ($j=3$) parts are thus separated. The shear waves may be propagating, corresponding to an imaginary $\nu$ with $\mathrm{Im}\,\nu\le 0$, or evanescent, corresponding to a real $\nu\ge 0$. Assuming that $\alpha$ is real as well, an analogous distinction can be made between propagating and evanescent compressional waves, in terms of $\gamma$. In principle, cross-terms between down- and up-going evanescent waves might still appear. Restriction is made, however, to regions, typically half-spaces, where such waves do not exist simultaneously. It follows that the contribution to $\mathcal{F}_z$ from the waves sharing a common $\mathbf{g}$ reduces to

$$\begin{aligned}
&\tfrac{\rho\omega\alpha^2}{2}\,(-\mathrm{Im}\,\gamma)\ \big(|A_{\mathbf{g}1+}|^2-|A_{\mathbf{g}1-}|^2\big)\ +\\
&\tfrac{\rho\omega\beta^2}{2}\,(-\mathrm{Im}\,\nu)\ \big(|A_{\mathbf{g}2+}|^2+|A_{\mathbf{g}3+}|^2-\\
&\qquad |A_{\mathbf{g}2-}|^2-|A_{\mathbf{g}3-}|^2\big)\ . \qquad (68)
\end{aligned}$$

Cross-terms from waves with different $\mathbf{g}$,$\mathbf{g}'$ involve $\exp\big(\mathrm{i}x(g_x-g'_x)+\mathrm{i}y(g_y-g'_y)\big)$ as a factor. Such terms disappear if an averaging over horizontal position is performed, to get $(\mathcal{F}_z)_{ave}$. The final result is

$$\begin{aligned}
&(\mathcal{F}_z)_{ave}=\\
&\tfrac{\rho\omega\alpha^2}{2}\,\textstyle\sum_{\mathbf{g}}\mathrm{Re}(K^+_{\mathbf{g}1z})\ \big(|A_{\mathbf{g}1+}|^2-|A_{\mathbf{g}1-}|^2\big)\ +\\
&\tfrac{\rho\omega\beta^2}{2}\,\textstyle\sum_{\mathbf{g}}\mathrm{Re}(K^+_{\mathbf{g}2z})\ \big(|A_{\mathbf{g}2+}|^2+|A_{\mathbf{g}3+}|^2-\\
&\qquad |A_{\mathbf{g}2-}|^2-|A_{\mathbf{g}3-}|^2\big). \qquad (69)
\end{aligned}$$

It should be observed that the assumptions of real $\alpha$ and $\beta$ imply a restriction to the elastic

case. Thus, application of Eq. (69) should typically be made in the water and steel half-spaces, and not in the rubber layer.

## APPENDIX B: CHANGE OF PULSE SHAPE WITH A NOTCH FILTER

A general function $g(t)$ of time $t$ is considered, with Fourier transform $G(\omega) = \int g(t) \exp(\mathrm{i}\omega t)\, dt$. It is the input to a linear filter with impulse function $h(t)$ and transfer function $H(\omega) = \int h(t) \exp(\mathrm{i}\omega t)\, dt$. Thus, the output is given by the convolution $(h*g)(t)$ with Fourier transform $H(\omega)G(\omega)$. It is assumed that $h(t)$ is real-valued, hence $H(-\omega) = H^*(\omega)$.

In the vicinity of $\pm\omega_0$, where $\omega_0$ is a certain positive angular frequency, $H(\omega)$ is now approximated by a linear function according to

$$\begin{aligned} H(\omega) \;\approx\; & a + \mathrm{i}\, b\, \mathrm{sgn}(\omega) + c\,(|\omega| - \omega_0) + \\ & \mathrm{i}\, d\,(\omega - \omega_0\, \mathrm{sgn}(\omega)) \;, \end{aligned} \tag{70}$$

where $a$,$b$,$c$,$d$ are the appropriate real constants. For a function $g(t)$ with spectrum concentrated to neighborhoods of $\pm\omega_0$ and Hilbert transform $(\mathcal{H}g)(t)$, it follows that

$$\begin{aligned} (h * g)(t) \;\approx\; & a\, g(t) - b\, (\mathcal{H}g)(t) - \\ & c\, \big((\mathcal{H}g)'(t) + \omega_0\, g(t)\big) - \\ & d\, \big(g'(t) - \omega_0\, (\mathcal{H}g)(t)\big) \;, \end{aligned} \tag{71}$$

which shows how the pulse shape of $g(t)$ is changed upon filtering. Eq. (71) is readily obtained from Eq. (70) by noting that the Fourier transforms of a derivative and a Hilbert transform are obtained by multiplication with $-\mathrm{i}\,\omega$ and $-\mathrm{i}\,\mathrm{sgn}(\omega)$, respectively.

For the particular case when $g(t)$ is a linear combination of the functions $\exp(+\mathrm{i}\omega_0 t)$ and $\exp(-\mathrm{i}\omega_0 t)$, it follows that $(\mathcal{H}g)'(t) + \omega_0\, g(t) \equiv 0$ and $g'(t) - \omega_0\, (\mathcal{H}g)(t) \equiv 0$. Hence,

$$(h * g)(t) \;\approx\; a\, g(t) - b\, (\mathcal{H}g)(t) \;. \tag{72}$$

A less trivial example of a function $g(t)$ with spectrum concentrated to the neighborhoods of $\pm\omega_0$ is furnished by $G(\omega) = \Phi(\omega - \omega_0) + \Phi(\omega + \omega_0)$, where $\Phi(\omega)$ is a real-valued, nonnegative, symmetrical function that is concentrated to a neighborhood of the origin. It follows that

$$g(t) \;=\; 2\, \cos(\omega_0 t)\, \varphi(t) \;, \tag{73}$$

where $\varphi(t)$ is the inverse Fourier transform of $\Phi(\omega)$. Apparently, $\varphi(t)$ is a real-valued and symmetrical function fulfilling $|\varphi(t)| \le \varphi(0)$ for all $t$. Hence, $\varphi'(0) = 0$, $\varphi(t)$ is approximatively constant in a neighborhood of the origin and Eq. (72) is applicable for small $t$. For a notch filter with $H(\pm\omega_0) = 0$, $a = b = 0$ and $(h * g)(t)$ becomes negligible for $t$ close to the origin. The apparent pulse splitting noted in the lower panel of Fig. 9 is thus explained.

## APPENDIX C: ABSORPTION AND SCATTERING CROSS-SECTIONS

Returning to the time-harmonic case, absorption and/or scattering cross-sections for scatterers in a bounded region with a surrounding homogeneous medium have been derived by several authors. [39, 7, 33, 40] In the present case, with a surrounding viscoelastic solid having a real compressional-wave velocity $\alpha$ and a possibly complex shear-wave velocity $\beta$, absorption loss may take place in the surrounding solid, not only within viscoelastic scatterers. Derivations for this case are included in this appendix.

The time-averaged power that is transferred into a sphere of radius $r$, centered at the origin and surrounding the scatterer region, can be expressed as

$$\mathcal{P}(r) \;=\; \int_{|\mathbf{r}|=r} \int \frac{\omega}{2}\, \mathrm{Im}\,(-\mathbf{T}(\mathbf{r}) \cdot \mathbf{u}^*(\mathbf{r}))\; dS(\mathbf{r}) \;, \tag{74}$$

where $dS(\mathbf{r})$ is the surface area element. As usual, $\mathbf{u}(\mathbf{r})$ is the displacement vector, and $\mathbf{T}(\mathbf{r})$ is the corresponding traction vector acting on a spherical surface with $|\mathbf{r}| = r$.

The wave field $\mathbf{u}(\mathbf{r})$ can be expanded in spherical waves according to

$$\begin{aligned} \mathbf{u}(\mathbf{r}) \;&=\; \sum_{Plm} a_{lm}^{0P} \mathbf{u}_{lm}^{0P}(\mathbf{r}) \;+\; \sum_{Plm} b_{lm}^{+P} \mathbf{u}_{lm}^{+P}(\mathbf{r}) \\ &=\; \sum_{Plm} \frac{1}{2} a_{lm}^{0P} \mathbf{u}_{lm}^{-P}(\mathbf{r}) \;+ \end{aligned} \tag{75}$$

$$\sum_{Plm}\left(\frac{1}{2}a_{lm}^{0P}+b_{lm}^{+P}\right)\mathbf{u}_{lm}^{+P}(\mathbf{r})\ , \qquad (76)$$

where the $a_{lm}^{0P}$ and $b_{lm}^{+P}$ coefficients concern the incident (including possible multiple-scattering contributions $b_{lm}^{\prime P}$, *cf.* Sec. III) and scattered fields, respectively. The basic vector wave functions $\mathbf{u}_{lm}^{-P}(\mathbf{r})$ are defined according to Eqs. (13)-(14) with $f_l$ chosen as the spherical Hankel function $\mathrm{h}_l^-$.

It is convenient to expand the basic solutions $\mathbf{u}_{lm}^{\pm P}(\mathbf{r})$ in a system of vector spherical harmonics that is complete and orthonormal over the surface of the unit sphere. With $\theta$,$\phi$ as the angular variables of $\mathbf{r}$, such a system is defined in equations (8.14) of Ref. [9]:

$$\mathbf{R}_l^m(\theta,\phi) = Y_l^m(\theta,\phi)\,\mathbf{e}_r(\mathbf{r}) \qquad (77)$$

$$\mathbf{S}_l^m(\theta,\phi) = \frac{1}{\sqrt{l(l+1)}}\left(\frac{\partial Y_l^m(\theta,\phi)}{\partial\theta}\,\mathbf{e}_\theta(\mathbf{r})+\frac{1}{\sin\theta}\frac{\partial Y_l^m(\theta,\phi)}{\partial\phi}\,\mathbf{e}_\phi(\mathbf{r})\right) \qquad (78)$$

$$\mathbf{T}_l^m(\theta,\phi) = \frac{1}{\sqrt{l(l+1)}}\left(\frac{1}{\sin\theta}\frac{\partial Y_l^m(\theta,\phi)}{\partial\phi}\,\mathbf{e}_\theta(\mathbf{r})-\frac{\partial Y_l^m(\theta,\phi)}{\partial\theta}\,\mathbf{e}_\phi(\mathbf{r})\right)\ . \qquad (79)$$

It is understood that $\mathbf{S}_0^0(\mathbf{r})$ and $\mathbf{T}_0^0(\mathbf{r})$ vanish identically. The expansions may be written

$$\mathbf{u}_{lm}^{\pm P}(\mathbf{r}) = U_l^{\pm P}(r)\mathbf{R}_l^m(\theta,\phi)+V_l^{\pm P}(r)\mathbf{S}_l^m(\theta,\phi)+W_l^{\pm P}(r)\mathbf{T}_l^m(\theta,\phi) \qquad (80)$$

along with analogous expansions

$$\mathbf{T}_{lm}^{\pm P}(\mathbf{r}) = R_l^{\pm P}(r)\mathbf{R}_l^m(\theta,\phi)+S_l^{\pm P}(r)\mathbf{S}_l^m(\theta,\phi)+T_l^{\pm P}(r)\mathbf{T}_l^m(\theta,\phi) \qquad (81)$$

of the corresponding traction vectors acting on a spherical surface with $|\mathbf{r}|=r$, needed for an expansion of $\mathbf{T}(\mathbf{r})$ similar to Eqs. (75)-(76). It follows from Eqs. (13)-(15), and equations (8.33)-(8.34) of Ref. [9], that

$$U_l^{\pm L}(r) = (\mathrm{h}_l^\pm)'(kr) \qquad (82)$$

$$V_l^{\pm L}(r) = \frac{\sqrt{l(l+1)}}{kr}\mathrm{h}_l^\pm(kr) \qquad (83)$$

$$R_l^{\pm L}(r) = \rho k\left((\frac{2\beta^2 l(l+1)}{(kr)^2}-\alpha^2)\mathrm{h}_l^\pm(kr)-\frac{4\beta^2(\mathrm{h}_l^\pm)'(kr)}{kr}\right) \qquad (84)$$

$$S_l^{\pm L}(r) = \frac{2\rho\beta^2\sqrt{l(l+1)}}{r}\left((\mathrm{h}_l^\pm)'(kr)-\mathrm{h}_l^\pm(kr)/kr\right) \qquad (85)$$

$$W_l^{\pm M}(r) = \mathrm{i}\,\mathrm{h}_l^\pm(k_s r) \qquad (86)$$

$$T_l^{\pm M}(r) = \mathrm{i}\rho\beta^2 k_s\left((\mathrm{h}_l^\pm)'(k_s r)-\frac{\mathrm{h}_l^\pm(k_s r)}{k_s r}\right) \qquad (87)$$

$$U_l^{\pm N}(r) = -\frac{\sqrt{l(l+1)}}{k_s r}\mathrm{h}_l^\pm(k_s r) \qquad (88)$$

$$V_l^{\pm N}(r) = -(\mathrm{h}_l^\pm)'(k_s r)-\mathrm{h}_l^\pm(k_s r)/k_s r \qquad (89)$$

$$R_l^{\pm N}(r) = -\frac{2\rho\beta^2\sqrt{l(l+1)}}{r}\left((\mathrm{h}_l^\pm)'(k_s r)-\mathrm{h}_l^\pm(k_s r)/k_s r\right) \qquad (90)$$

$$S_l^{\pm N}(r) = \rho\beta^2 k_s\left((1-\frac{2l(l+1)-2}{(k_s r)^2})\mathrm{h}_l^\pm(k_s r)+\frac{2(\mathrm{h}_l^\pm)'(k_s r)}{k_s r}\right)\ . \qquad (91)$$

The wavenumbers $k$ and $k_s$ appearing here are defined as $k=\omega/\alpha$ and $k_s=\omega/\beta$, respectively. Furthermore, $\rho$ is the density of the surrounding medium, and $\mu=\rho\beta^2$ is its shear modulus. The remaining functions $W_l^{\pm L}(r)$,$T_l^{\pm L}(r)$, $U_l^{\pm M}(r)$,$V_l^{\pm M}(r)$,$R_l^{\pm M}(r)$,$S_l^{\pm M}(r)$, and $W_l^{\pm N}(r)$,$T_l^{\pm N}(r)$ vanish identically.

By exploiting the orthonormality properties of $\mathbf{R}_l^m(\theta,\phi)$, $\mathbf{S}_l^m(\theta,\phi)$ and $\mathbf{T}_l^m(\theta,\phi)$, $\mathcal{P}(r)$ from Eq. (74) can be expressed as

$$\begin{aligned}\mathcal{P}(r) = {}& -\tfrac{\omega r^2}{2}\textstyle\sum_{lm}\mathrm{Im}\Big[\Big(\sum_P \frac{a_{lm}^{0P}}{2}R_l^{-P}(r)+\sum_P(\frac{a_{lm}^{0P}}{2}+b_{lm}^{+P})R_l^{+P}(r)\Big)\cdot\\ &\Big(\sum_P \tfrac{a_{lm}^{0P}}{2}U_l^{-P}(r)+\sum_P(\tfrac{a_{lm}^{0P}}{2}+b_{lm}^{+P})U_l^{+P}(r)\Big)^*+\\ &\Big(\sum_P \tfrac{a_{lm}^{0P}}{2}S_l^{-P}(r)+\sum_P(\tfrac{a_{lm}^{0P}}{2}+b_{lm}^{+P})S_l^{+P}(r)\Big)\cdot\\ &\Big(\sum_P \tfrac{a_{lm}^{0P}}{2}V_l^{-P}(r)+\sum_P(\tfrac{a_{lm}^{0P}}{2}+b_{lm}^{+P})V_l^{+P}(r)\Big)^*+\\ &\Big(\sum_P \tfrac{a_{lm}^{0P}}{2}T_l^{-P}(r)+\sum_P(\tfrac{a_{lm}^{0P}}{2}+b_{lm}^{+P})T_l^{+P}(r)\Big)\cdot\\ &\Big(\sum_P \tfrac{a_{lm}^{0P}}{2}W_l^{-P}(r)+\end{aligned}$$

$$\sum_P (\tfrac{a_{lm}^{0P}}{2} + b_{lm}^{+P}) W_l^{+P}(r) \Big)^* \Big] \,. \quad (92)$$

Eqs. (74)-(92) are valid for general $\alpha$. The restriction to a real $\alpha$ is made from now on, as is the restriction to a compressional incident wave. Hence, $a_{lm}^{0M} = a_{lm}^{0N} = 0$ for all $lm$.

For large $r$, it follows by applying standard asymptotic expressions for spherical Hankel functions, and neglecting terms of magnitude $\mathcal{O}(r^{-2})$, that

$$\begin{aligned} U_l^{\pm L}(r) &\sim (\mp \mathrm{i})^l \exp(\pm \mathrm{i}kr)/kr & (93)\\ R_l^{\pm L}(r) &\sim -(\mp \mathrm{i})^{l+1} \rho\alpha^2 \exp(\pm \mathrm{i}kr)/r & (94)\\ W_l^{+M}(r) &\sim -V_l^{+N}(r) \\ &\sim (-\mathrm{i})^l \exp(\mathrm{i}k_s r)/k_s r & (95)\\ T_l^{+M}(r) &\sim -S_l^{+N}(r) \\ &\sim -(-\mathrm{i})^{l+1} \rho\beta^2 \exp(\mathrm{i}k_s r)/r, & (96) \end{aligned}$$

while all remaining components are either irrelevant or negligible. For the anelastic case, with $\mathrm{Im}(k_s) > 0$, the components in Eqs. (95)-(96) are negligible as well.

Substitution in Eq. (92) reveals that all coupling terms disappear when the imaginary part has been isolated, between "$-L$" and "$+L$" terms, as well as between terms of different $P = L,M,N$ types. For the anelastic case,

$$\lim_{r\to\infty} \mathcal{P}(r) \;=\; \tfrac{\rho\alpha^3}{2} \cdot \sum_{l=0}^{\infty} \sum_{m=-l}^{l} |b_{lm}^{+L}|^2 \left[ -1 - \mathrm{Re}\left( \tfrac{a_{lm}^{0L}}{b_{lm}^{+L}} \right) \right] \quad (97)$$

is obtained, while the elastic case with its vanishing absorption provides the relation

$$\tfrac{\rho\alpha^3}{2} \sum_{l=0}^{\infty} \sum_{m=-l}^{l} |b_{lm}^{+L}|^2 \left[ -1 - \mathrm{Re}\left( \tfrac{a_{lm}^{0L}}{b_{lm}^{+L}} \right) \right] = \tfrac{\rho\beta^3}{2} \sum_{P=M,N} \sum_{l=0}^{\infty} \sum_{m=-l}^{l} |b_{lm}^{+P}|^2 \,. \quad (98)$$

The power in outgoing scattered compressional waves is readily identified as

$$\frac{\rho\alpha^3}{2} \sum_{l=0}^{\infty} \sum_{m=-l}^{l} |b_{lm}^{+L}|^2 \,. \quad (99)$$

In the elastic case, the power

$$\frac{\rho\beta^3}{2} \sum_{P=M,N} \sum_{l=0}^{\infty} \sum_{m=-l}^{l} |b_{lm}^{+P}|^2 \quad (100)$$

in outgoing, scattered shear waves also remains at large $r$.

Absorption and scattering cross-sections are obtained from Eqs. (97) and (99)-(100), respectively, by dividing with the intensity of the incident compressional wave. The typical case is a plane wave of unit displacement amplitude, for which the intensity is $\rho\alpha\omega^2/2$. For an isolated spherical scatterer of radius $a$, a further division with the geometrical cross-section $\pi a^2$ provides dimensionless normalized cross-sections. The extinction cross-section, [33] defined as the sum of the absorption and scattering cross-sections, represents the total redistribution of power from the incident wave field, in relation to the incident intensity.

The truncation for the example case of Sec. VI implies, in particular, a restriction to the spherically symmetric part of the wave field around each cavity. For such a wave field, of the type $\mathbf{u}(\mathbf{r}) = u(r) \cdot \mathbf{e}_r$, the function $\mathcal{P}'(r)/4\pi r^2$ represents the time-averaged strain power density at $r$, which can be explicitly expressed as[41]

$$\begin{aligned} &-\tfrac{\omega}{2} \mathrm{Im}\left( \tau^{rr} (e^{rr})^* + \tau^{\theta\theta} (e^{\theta\theta})^* + \right. \\ &\qquad \left. \tau^{\phi\phi} (e^{\phi\phi})^* \right) = & (101)\\ &-\tfrac{\omega}{2} \mathrm{Im}\left( \tau^{rr} (e^{rr} + e^{\theta\theta} + e^{\phi\phi})^* + \right. \\ &\qquad \left. 4\mu \left( \tfrac{u}{r} - \tfrac{\partial u}{\partial r} \right) \tfrac{u^*}{r} \right) \,. & (102) \end{aligned}$$

Here, $\tau^{rr}$,$\tau^{\theta\theta}$,$\tau^{\phi\phi}$ and $e^{rr}$,$e^{\theta\theta}$,$e^{\phi\phi}$ are the indicated spherical components of the stress and strain tensors, respectively. For the case of a spherical cavity with radius $a$ centered at the origin, $\tau^{rr}(a) = 0$ and $\mathrm{Im}(-\mu)$ appears as a factor for the strain power density at $r = a$.

For the particular case of a homogeneous medium without scatterers, and a regular spherical wave $\mathbf{u}(\mathbf{r}) = \mathbf{u}_{lm}^{0L}(\mathbf{r})$, some elementary calculations with $\mathrm{j}_0(kr)$ and $\mathrm{h}_0^+(kr)$ provide the asymptotic expression

$$\frac{\rho\omega|k|^2}{8\pi} \mathrm{Im}\left( \frac{4}{3}\beta^2 - \alpha^2 \right) \quad (103)$$

for the strain power density as $r$ tends to zero. A complex $\alpha$ is here allowed again and, indeed, $\mathrm{Im}(-\alpha^2) \geq 4\,\mathrm{Im}(-\beta^2)/3$ is required in order to fulfil the physical requirement of a nonnegative strain power density. This is only the

well known condition of a nonpositive imaginary part for the bulk modulus. [41]

For the examples of Secs. V and VI, for example, a compressional-wave absorption in the rubber of about 0.06 dB/wavelength would actually be needed. This is quite insignificant, however, and the use of a real $\alpha$ in this paper is justified. It has facilitated the theoretical analysis considerably, and the discussion of cross-sections would have been less clear with absorption loss already in an incident compressional plane wave.

## References


[1] H. Oberst, "Resonant sound-absorbers," in *Technical Aspects of Sound*, edited by E.G. Richardson (Elsevier, Amsterdam, 1957), Chap. 7, pp. 287-327.

[2] G. Gaunaurd and H. Überall, "Theory of resonant scattering from spherical cavities in elastic and viscoelastic media," J. Acoust. Soc. Am. **63**, 1699-1712 (1978).

[3] G. Gaunaurd, K.P. Scharnhorst, and H. Überall, "Giant monopole resonances in the scattering of waves from gas-filled spherical cavities and bubbles," J. Acoust. Soc. Am. **65**, 573-594 (1979).

[4] G. Gaunaurd, "Comments on 'Absorption mechanisms for waterborne sound in Alberich anechoic layers'," Ultrasonics **23**, 90-91 (1985).

[5] D. Brill and G. Gaunaurd, "Resonance theory of elastic waves ultrasonically scattered from an elastic sphere," J. Acoust. Soc. Am. **81**, 1-21 (1987).

[6] E. Meyer, K. Brendel, and K. Tamm, "Pulsation oscillations of cavities in rubber," J. Acoust. Soc. Am. **30**, 1116-1120 (1958).

[7] V.A. Korneev and L.R. Johnson, "Scattering of P and S waves by a spherically symmetric inclusion," PAGEOPH **147**, 675-718 (1996).

[8] F. Jensen, W. Kuperman, M. Porter, and H. Schmidt, *Computational Ocean Acoustics* (AIP Press, New York, 1994).

[9] K. Aki and P. Richards, *Quantitative Seismology* (Univ. Science Books, Sausalito, 2002).

[10] H. Strifors and G. Gaunaurd, "Selective reflectivity of viscoelastically coated plates in water," J. Acoust. Soc. Am. **88**, 901-910 (1990).

[11] A.N.P. Cederholm and I. Karasalo, "Inverse modelling of rubber coated steel plates with a genetic algorithm," Acta Acustica united with Acustica **88**, 694-698 (2002).

[12] A.-C. Hladky-Hennion and J.-N. Decarpigny, "Analysis of the scattering of a plane wave by a doubly periodic structure using the finite element method: application to Alberich anechoic coatings," J. Acoust. Soc. Am. **90**, 3356-3367 (1991).

[13] A.-C. Hladky-Hennion and J.-N. Decarpigny, "Note on the validity of using plane-wave type relations to characterize Alberich anechoic coatings," J. Acoust. Soc. Am. **92**, 2878-2882 (1992).

[14] V. Easwaran and M.L. Munjal, "Analysis of reflection characteristics of a normal incidence plane wave on resonant sound absorbers: a finite element approach," J. Acoust. Soc. Am. **93**, 1308-1318 (1993).

[15] Z. Liu, C.T. Chan, P. Sheng, A.L. Goertzen, and J.H. Page, "Elastic wave scattering by periodic structures of spherical objects: theory and experiment," Phys. Rev. B **62**, 2446-2457 (2000).

[16] I.E. Psarobas, N. Stefanou, and A. Modinos, "Scattering of elastic waves by periodic arrays of spherical bodies," Phys. Rev. B **62**, 278-291 (2000).

[17] N. Stefanou, V. Yannopapas, and A. Modinos, "Multem2: a new version of the program for transmission and band-structure calculations of photonic crystals," Comput. Phys. Comm. **132**, 189-196 (2000).

[18] B.L.N. Kennett, *Seismic Wave Propagation in Stratified Media* (Cambridge Univ. Press, Cambridge, 1983).

[19] J.B. Pendry, *Low Energy Electron Diffraction* (Academic Press, London, 1974).

[20] A. Boström, On the systematic use of spherical, cylindrical and plane vector wave functions, 2002, in *Acoustic Interactions with Submerged Elastic Structures, Part IV*, A. Guran, A. Boström, O. Leroy and G. Maze (ed.), 41-79.

[21] G. Gaunaurd and J. Barlow, "Matrix viscosity and cavity-size distribution effects on the dynamic effective properties of perforated elastomers," J. Acoust. Soc. Am. **75**, 23-34 (1984).

[22] S. Ivansson, "Solving ODE boundary-value problems: safe compound-matrix dimension reduction with the Riccati method," Int. J. Diff. Eq. Applic. **5**, 339-352 (2002).

[23] K. Maslov, V.K. Kinra, and B.K. Henderson, "Lattice resonances of a planar array of spherical inclusions: an experimental study," Mech. Mater. **31**, 175-186 (1999).

[24] G.R. Fowles, *Introduction to Modern Optics* (Holt, Rinehart and Winston, New York, 1975).

[25] S. Ivansson and I. Karasalo, "Computation of modal wavenumbers using an adaptive winding-number integral method with error control," J. Sound Vib. **161**, 173-180 (1993).

[26] K. Maslov and V.K. Kinra, "Acoustic response of a periodic layer of nearly rigid spherical inclusions in an elastic solid," J. Acoust. Soc. Am. **106**, 3081-3088 (1999).

[27] K. Maslov, V.K. Kinra, and B.K. Henderson, "Elastodynamic response of a coplanar periodic layer of elastic spherical inclusions," Mech. Mater. **32**, 785-795 (2000).

[28] M.S. Kushwaha and P. Halevi, "Stop bands for cubic arrays of spherical balloons," J. Acoust. Soc. Am. **101**, 619-622 (1997).

[29] J.N. Munday, C.B. Bennett, and W.M. Robertson, "Bands gaps and defect modes in periodically structured waveguides," J. Acoust. Soc. Am. **112**, 1353-1358 (2002).

[30] B.A. Munk, *Frequency Selective Surfaces* (Wiley, New York, 2000).

[31] A.D. Pierce, *Acoustics* (Acoustical Society of America, New York, 1991).

[32] R. Matsunaga, T. Kikuchi, A. Hasegawa, and S. Takahashi, "Multiple scattering effects of doublet cavities in rubber," Japanese J. Appl. Physics **30-1**, 102-104 (1991).

[33] H. Medwin and C.S. Clay, *Acoustical Oceanograpy* (Academic Press, Boston, 1998).

[34] I. Tolstoy and A. Tolstoy, "Line and plane arrays of monopole scatterers," J. Acoust. Soc. Am. **87**, 1038-1043 (1990).

[35] F.G. Blake, "Spherical wave propagation in solid media," J. Acoust. Soc. Am. **24**, 211-215 (1952).

[36] S. Ivansson, "Riccati-method modelling of echo reduction by Alberich anechoic coatings," on the CD-ROM: *Proc. UDT Europe 2003 (Undersea Defence Technology).*

[37] R.H. Hackman, "The transition matrix for acoustic and elastic wave scattering in prolate spheroidal coordinates," J. Acoust. Soc. Am. **75**, 35-45 (1984).

[38] J.A. Hudson, *The Excitation and Propagation of Elastic Waves* (Cambridge Univ. Press, Cambridge, 1980).

[39] P.M. Morse and K.U. Ingard, *Theoretical Acoustics* (McGraw-Hill, New York, 1968).

[40] I.E. Psarobas, "Viscoelastic response of sonic band-gap materials," Phys. Rev. B **64**, 012303/1-4 (2001).

[41] S. Ivansson, "Shear-wave induced transmission loss in a fluid-solid medium," J. Acoust. Soc. Am. **96**, 2870-2875 (1994). Correction: replace 1/4 by 1/2 in (18) and (21).